iScience

CellPress
OPEN ACCESS

Article

Preclinical safety and efficacy of a therapeutic antibody that targets SARS-CoV-2 at the sotrovimab face but is escaped by Omicron

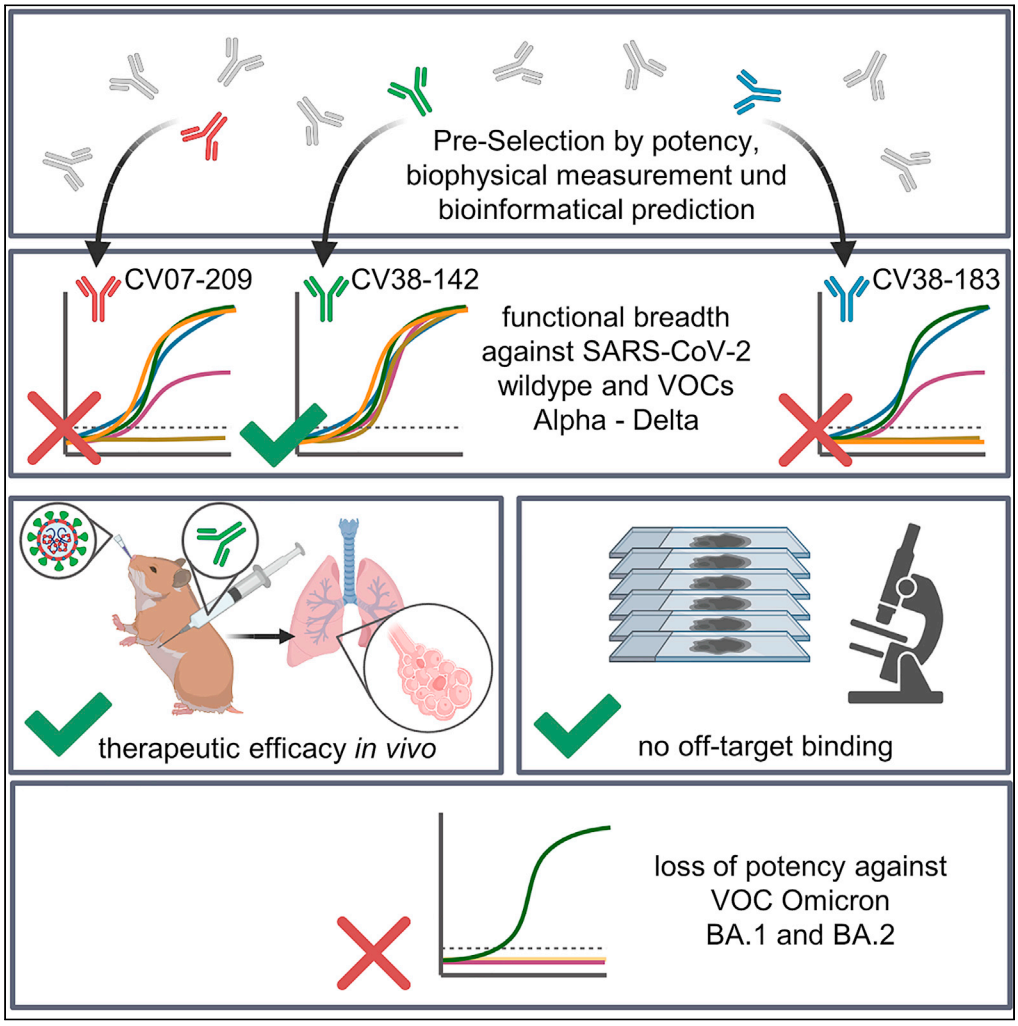

Jakob Kreye, S. Momsen Reincke, Stefan Edelburg, ..., Uwe Janssen, Victor M. Corman, Harald Prüss

jakob.kreye@dzne.de (J.K.)
momsen.reincke@dzne.de (S.M.R.)
harald.pruess@dzne.de (H.P.)

Highlights

Antibody CV38-142 neutralizes wild-type SARS-CoV-2 and VOC Alpha, Beta, Gamma, Delta

Post-exposure and therapeutic efficacy in hamster model of VOC infection

No off-target binding in human protein library and tissue cross-reactivity study

No neutralization of Omicron led to discontinuation of clinical development

Kreye et al., iScience 26, 106323
April 21, 2023
https://doi.org/10.1016/j.isci.2023.106323

iScience

CellPress
OPEN ACCESS

Article

Preclinical safety and efficacy of a therapeutic antibody that targets SARS-CoV-2 at the sotrovimab face but is escaped by Omicron

Jakob Kreye,[1,2,3,4,5,19,20,*] S. Momsen Reincke,[1,2,3,5,19,*] Stefan Edelburg,[6] Lara M. Jeworowski,[7,8] Hans-Christian Kornau,[1,9] Jakob Trimpert,[10] Peter Hombach,[6] Sophia Halbe,[6] Volker Nölle,[6] Martin Meyer,[6] Stefanie Kattenbach,[6] Elisa Sánchez-Sendin,[1,2,3] Marie L. Schmidt,[7,8] Tatjana Schwarz,[7,8] Ruben Rose,[11] Andi Krumbholz,[11,12] Sophie Merz,[13] Julia M. Adler,[10] Kathrin Eschke,[10] Azza Abdelgawad,[10] Dietmar Schmitz,[1,9,14,15,16] Leif E. Sander,[17] Uwe Janssen,[6] Victor M. Corman,[5,7,8,18] and Harald Prüss[1,2,3,*]

SUMMARY

The recurrent emerging of novel viral variants of concern (VOCs) with evasion of preexisting antibody immunity upholds severe acute respiratory syndrome coronavirus 2 (SARS-CoV-2) case numbers and maintains a persistent demand for updated therapies. We selected the patient-derived antibody CV38-142 based on its potency and breadth against the VOCs Alpha, Beta, Gamma, and Delta for preclinical development into a therapeutic. CV38-142 showed *in vivo* efficacy in a Syrian hamster VOC infection model after post-exposure and therapeutic application and revealed a favorable safety profile in a human protein library screen and tissue cross-reactivity study. Although CV38-142 targets the same viral surface as sotrovimab, which maintains activity against Omicron, CV38-142 did not neutralize the Omicron lineages BA.1 and BA.2. These results highlight the contingencies of developing antibody therapeutics in the context of antigenic drift and reinforce the need to develop broadly neutralizing variant-proof antibodies against SARS-CoV-2.

INTRODUCTION

The COVID-19 pandemic drastically impacts global life and has already resulted in severe consequences including millions of cases of death, a largely unknown magnitude of long-term post-COVID health sequelae, and prolonged restrictions in economic, social, and cultural activities. While in many parts of the world the immunization rates increase with the broad availability of multiple vaccines, the global incidences maintain at high levels as novel viral variants of concern (VOC) continuously emerge, some of which are associated with enhanced viral transmission[2,3] or increased resistance to antibodies from previous infections or vaccinations.[4–7] Together with vaccine hesitancy at relevant frequencies in many countries[8] and a significantly reduced immune response to vaccinations in immunocompromised patients,[9] this underlines the persistent need for a broad variety of therapeutic agents to dampen the consequences of the SARS-CoV-2 infections. Of those, antibody-based therapies have been shown as a promising approach with short development times, efficacy in the reduction of disease severity and hospitalization rates,[10,11] and the flexibility for different application pathways.[12,13] Ideal therapeutic monoclonal antibodies (mAbs) against SARS-CoV-2 feature high neutralization potency, a robust safety profile, and enhanced efficacy breadth against all relevant viral variants and preferably also against further coronaviridae. The applicability of such therapeutic mAbs can be jeopardized by changes in the regional or global distribution of circulating VOCs, as exemplified by the emergence of the Omicron lineage BA.1 in late 2021. BA.1 is resistant to most mAb therapies that were authorized by the Food and Drug Administration (FDA) or European Medicines Agency (EMA) at that time.[3,14,15] In contrast, the authorized therapeutic mAb sotrovimab,[11] which was isolated from a SARS-CoV-infected individual[16] and initially named S309, retained its activity against BA.1[3] via binding to a conserved viral epitope.[16,17] However, sotrovimab's applicability has been affected by the recently emerged Omicron sublineage BA.2 that quickly became the dominating variant in many parts of the world as sotrovimab's neutralizing activity is 27-fold reduced against BA.2.[18] This demonstrates the necessity to continuously develop novel therapeutic mAbs for the containment of SARS-CoV-2.

[1]German Center for Neurodegenerative Diseases (DZNE) Berlin, 10117 Berlin, Germany

[2]Helmholtz Innovation Lab BaoBab (Brain Antibody-omics and B-cell Lab), 10117 Berlin, Germany

[3]Department of Neurology and Experimental Neurology, Charité-Universitätsmedizin Berlin, Corporate Member of Freie Universität Berlin, Humboldt-Universität Berlin, and Berlin Institute of Health, 10117 Berlin, Germany

[4]Department of Pediatric Neurology, Charité-Universitätsmedizin Berlin, Corporate Member of Freie Universität Berlin, Humboldt-Universität Berlin, and Berlin Institute of Health, 10117 Berlin, Germany

[5]Berlin Institute of Health at Charité, Charité-Universitätsmedizin Berlin, 10117 Berlin, Germany

[6]Miltenyi Biotec B.V. & Co. KG, 51429 Bergisch Gladbach, Germany

[7]Institute of Virology, Charité-Universitätsmedizin Berlin, Corporate Member of Freie Universität Berlin, Humboldt-Universität zu Berlin, and Berlin Institute of Health, 10117 Berlin, Germany

[8]German Centre for Infection Research (DZIF), 10117 Berlin, Germany

[9]Neuroscience Research Center (NWFZ), Charité-Universitätsmedizin Berlin, Corporate Member of Freie Universität Berlin, Humboldt-Universität Berlin, and Berlin Institute of Health, 10117 Berlin, Germany

Continued

From peripheral blood of early pandemic convalescent COVID-19 patients, we previously isolated 598 mAbs and identified 18 mAbs with the highest potency to neutralize authentic wild-type SARS-CoV-2.[1] Here, we present the systematic selection and preclinical characterization of CV38-142. This mAb binds SARS-CoV-2 to a conserved sarbecovirus epitope with overlap of the sotrovimab (S309) site,[19] thereby exhibiting broad functional breadth.[20]

RESULTS

Selection of lead candidates for therapeutic antibody development

From the selection of 18 potent SARS-CoV-2 neutralizing mAbs and based on their previously characterized superior functional properties[1] combined with the here-analyzed biophysical and bioinformatical parameters predictive for favorable developability, we selected the mAbs CV07-209, CV38-183, and CV38-142 as candidates for further development (Figure 1A). CV38-142 exhibited neutralizing potency not only against SARS-CoV-2 but also against SARS-CoV.[19] Additional analyses revealed that, of 100 previously isolated SARS-CoV-2 receptor-binding domain (RBD) mAbs,[1] eight including CV38-142 also bound to SARS-CoV RBD (not shown), confirming that cross-reactivity to SARS-CoV is a rare feature among RBD mAbs elicited after SARS-CoV-2 infection.[21,22] Of these eight antibodies, we found two with similar dose-dependent binding to SARS-CoV RBD as CV38-142 (Figure 1B). Whereas one of these two (CV07-214) partially competed with CV38-142 for binding to the RBD of both viruses, the other one (CV38-115) bound to an independent site (Figure 1C). Of those three, only CV38-142 showed potent neutralization of authentic SARS-CoV-2 (Figure 1D).

Broad potency of CV38-142 against SARS-CoV-2 variants of concern

For recombinant production of the three selected mAbs CV07-209, CV38-183, and CV38-142, stable Chinese hamster ovary (CHO) cell lines were generated using lentiviral transduction and single-cell cloning from enriched high-producer cell pools to ensure monoclonality following good manufacturing practice (GMP) guidelines. mAbs purified from CHO cell culture supernatant showed *in vitro* neutralization of authentic wild-type SARS-CoV-2 comparable to mAbs from transient production in human embryonic kidney (HEK)-293T cells used during the antibody selection process (Figures S1A–S1C). To confirm the correct assembly of antibodies and exclude the presence of undesired species such as heavy-chain dimers, we analyzed deglycosylated antibodies using mass spectrometry. mAbs derived from CHO cell lines had the expected molecular mass (Figures S1D–S1F and S1M), showed favorable conformational stability as determined by nano differential scanning fluorimetry (Figures S1G–S1I and S1M), and did not form aggregates as verified by size exclusion chromatography (Figures S1J–S1M). Consequently, for all experiments thereafter, mAbs derived from CHO cell lines were used. In surface plasmon resonance (SPR) measurements, all three mAbs showed high affinity binding to SARS-CoV-2 RBD with equilibrium dissociation constants (K_D) between 12.5 p.m. and 1.04 nM (Figures 2A–2C). Both CV07-209 and CV38-183 competed with the binding of the RBD to its host receptor angiotensin-converting enzyme 2 (ACE2) with a half-maximal competition at 2.8 and 3.4 nM, respectively (Figures S2A–S2C and 2D). In contrast, CV38-142 did not interfere with the ACE2-RBD interaction (Figure 2D), in line with structural data that characterized the CV38-142 epitope to be distinct from the ACE2 interaction site.[19] To elucidate the functional breadth of the mAbs, we performed solid-phase assays and authentic virus plaque reduction neutralization tests (PRNT) with all VOCs present at that time (Alpha, Beta, Gamma, and Delta). While the binding and neutralizing activity of CV07-209 and CV38-183 to Beta and Gamma was drastically reduced or not detectable (Figures 2E–2G), CV38-142 revealed potency against the wild-type virus and all four tested VOCs (Figures 2E and 2H). Taken together, CV38-142 showed the greatest functional breadth in the *in vitro* experiments and was therefore selected as the lead mAb candidate.

Therapeutic efficacy in a SARS-CoV-2 VOC infection model in hamsters

Next, we used the COVID-19 disease model in Syrian hamsters[24,25] to evaluate the *in vivo* efficacy of CV38-142 to protect from lung pathology after infection with a SARS-CoV-2 VOC. The animals were first infected with an authentic SARS-CoV-2 Alpha isolate via intranasal application and then received a single intraperitoneal injection of 30 mg/kg of mAb CV38-142 either 2 h (post-exposure group) or 24 h post-infection (therapeutic group) (Figure 3A). Animals that had received an isotype-matched non-antiviral mAb (control group) showed a gradual decrease in weight, the primary clinical sign of SARS-CoV-2-induced disease in Syrian hamsters,[26] with a maximum loss of more than 15% at the end of the observational period at seven days post-infection (dpi). In contrast, hamsters of the post-exposure and

[10]Institute of Virology, Freie Universität Berlin, 14163 Berlin, Germany

[11]Institute for Infection Medicine, Christian-Albrechts-Universität zu Kiel and University Medical Center Schleswig-Holstein, 24105 Kiel, Germany

[12]Labor Dr. Krause & Kollegen MVZ GmbH, 24106 Kiel, Germany

[13]IDEXX Laboratories, 70806 Kornwestheim, Germany

[14]Einstein Center for Neuroscience, Charité-Universitätsmedizin Berlin, Corporate Member of Freie Universität Berlin, Humboldt-Universität Berlin, and Berlin Institute of Health, 10117 Berlin, Germany

[15]NeuroCure Cluster of Excellence, Charité-Universitätsmedizin Berlin, Corporate Member of Freie Universität Berlin, Humboldt-Universität Berlin, and Berlin Institute of Health, 10117 Berlin, Germany

[16]Bernstein Center for Computational Neuroscience, Humboldt-Universität zu Berlin, 10115 Berlin, Germany

[17]Department of Infectious Diseases and Respiratory Medicine, Charité-Universitätsmedizin Berlin, Corporate Member of Freie Universität Berlin, Humboldt-Universität Berlin, and Berlin Institute of Health, 10117 Berlin, Germany

[18]Labor Berlin-Charité Vivantes GmbH, Berlin, Germany

[19]These authors contributed equally

[20]Lead contact

*Correspondence: jakob.kreye@dzne.de (J.K.), momsen.reincke@dzne.de (S.M.R.), harald.pruess@dzne.de (H.P.)

https://doi.org/10.1016/j.isci.2023.106323

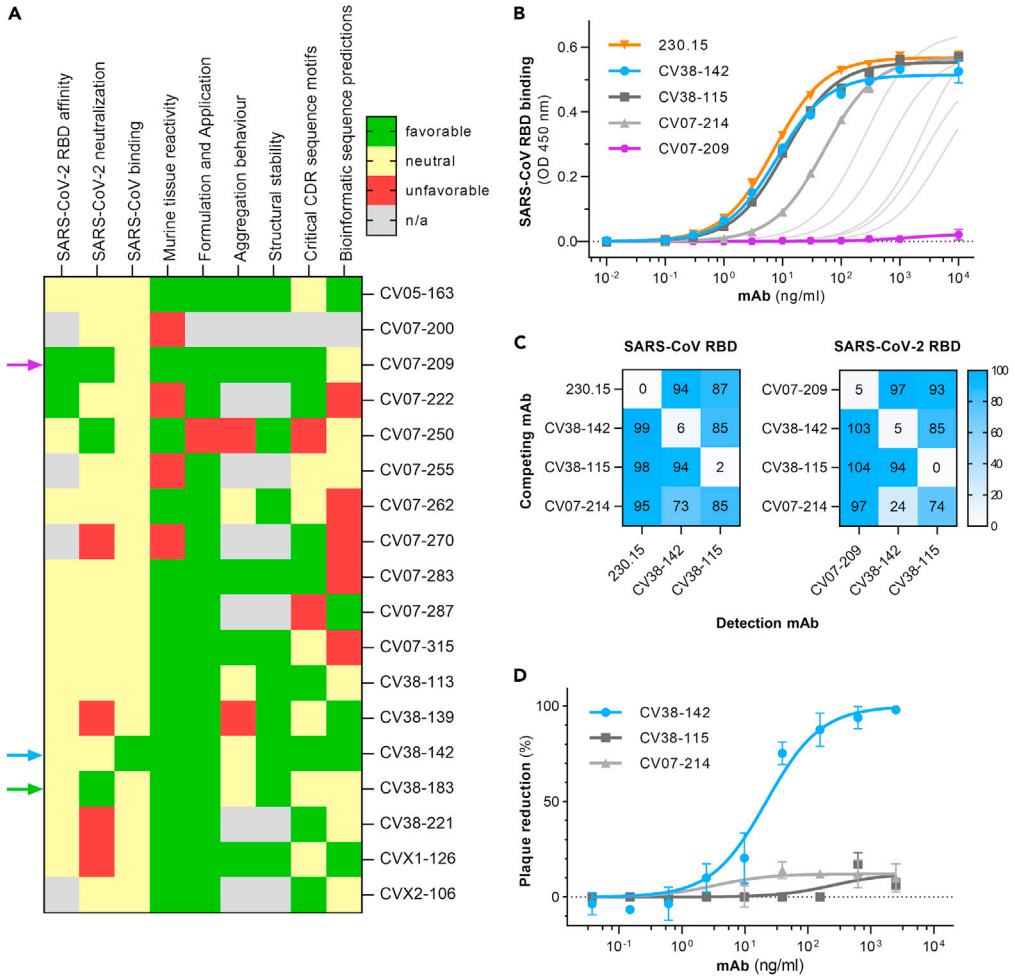

Figure 1. Predictions of mAb developability and SARS-CoV cross-reactivity

(A) An evaluation of functional, biophysical, and bioinformatical parameters of mAbs regarding their translational potential for the development into a therapeutic antibody. The 18 indicated mAbs had previously been identified by their high potency for SARS-CoV-2 neutralization from 598 mAbs isolated from COVID-19 convalescent patients.[1] The functional parameters SARS-CoV-2 RBD affinity (as measured by surface plasmon resonance), SARS-CoV-2 neutralization (authentic wild-type virus plaque reduction neutralization tests), SARS-CoV binding (RBD ELISA), and murine tissue reactivity (immunohistochemistry) have been investigated previously.[1] The biophysical and bioinformatical parameters, formulation and application (isoelectric focusing), aggregation behavior (size exclusion chromatography), structural stability (nano differential scanning fluorimetry), critical CDR sequence motifs, and bioinformatic sequence predictions, were analyzed for this manuscript and are displayed in Table S1. Criteria for classification as favorable, neutral, or unfavorable for all parameters are described in the STAR Methods section. The three selected mAb candidates for further development are indicated with arrows next to the heatmap. n/a = not available.

(B) Concentration-dependent binding of the indicated mAbs to fusion proteins containing the SARS-CoV RBD and the Fc region of rabbit IgG revealed by ELISA. mAb 230.15 was isolated from a convalescent SARS-CoV-infected individual.[23] The other mAbs were isolated from convalescent SARS-CoV-2-infected individuals[1] and identified to cross-react with SARS-CoV RBD. Non-linear regression models are shown. Values indicate mean ± SD from two wells of one experiment.

(C) Competition of mAbs for binding to the RBD of the indicated virus. Shades of blue and numbers in each tile indicate the percent RBD binding of detection mAb in presence of 100-fold excess of competing mAb relative to non-competition conditions as revealed by RBD-Fc ELISA. Blue squares indicate no competition. Biotinylation interfered with the reactivity of CV07-214 precluding its use as a detection antibody. Data are shown as mean of two independent experiments.

(D) Concentration-dependent neutralization of plaque formation from authentic wild-type SARS-CoV-2 isolate by indicated mAbs. Non-linear regression models are shown. Values indicate mean ± SD from two independent measurements. See also Table S1.

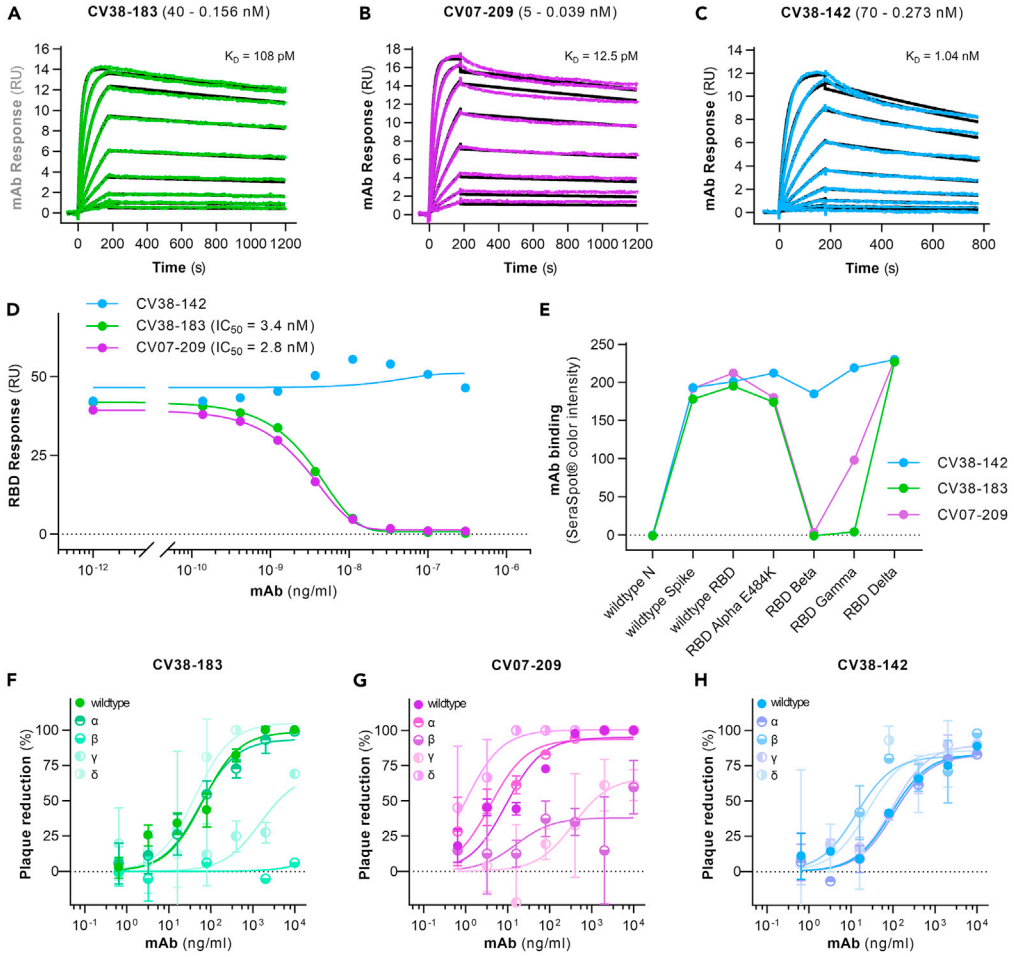

Figure 2. Affinity and potency breadth of SARS-CoV-2-neutralizing candidate mAbs

(A–C) Binding kinetics of mAbs to SARS-CoV-2 wild-type RBD were modeled (black) from multi-cycle SPR measurements (green, purple, blue). All measurements were performed in duplicates and by using a serial 2-fold dilution of mAbs in the indicated range on reversibly immobilized SARS-CoV-2-S1 RBD-mFc. The K_D values were determined using a monovalent analyte model and are shown above the graphs.

(D) Competition of mAbs with RBD-ACE2 interaction as quantified by the mAb concentration-dependent RBD response on an immobilized Avi-tagged ACE2 protein using SPR. All measurements were performed in duplicates and the responses analyzed using non-linear regression models. mAb concentrations of half-maximal competition of the RBD-ACE2 interaction (IC_{50}) are shown from non-linear regression models, if available.

(E) Binding of the indicated mAbs at 2 μg/mL to SARS-CoV-2 RBD constructs of wild-type or the indicated VOCs or to control (Nucleocapsid (N) protein) shown as color intensity measurements of a solid-phase binding assay.

(F–H) Concentration-dependent neutralization of plaque formation from authentic SARS-CoV-2 of wild-type or VOC isolates by mAbs. Non-linear regression models are shown. Values indicate mean ± SD from two technical duplicates.

See also Figures S1 and S2 and Table S1.

therapeutic groups nearly maintained their starting weight throughout the experiment (Figure 3B). qPCR measurements of viral genomic RNA in the upper airways as measured from throat swabs revealed similar results from all groups at three, five, and seven dpi (Figure 3C). However, in lung tissues from all time points, viral RNA levels showed a 2–3 log reduction in animals that had received CV38-142 in comparison to controls (Figure 3D). Similarly, functional SARS-CoV-2 particles were reduced in the respective lung homogenates with the plaque-forming unit (PFU) count below the detection threshold for most hamsters of the post-exposure and therapeutic groups (Figure 3E). To evaluate the effects of CV38-142 on the SARS-CoV-2 VOC-mediated lung pathology, the tissues were histopathologically examined at all time points by board-certified veterinary pathologists (Table S2). The control group lungs exhibited typical signs of viral pneumonia with immune cell infiltration, alveolar epithelial cell (AEC) type II hyperplasia, and

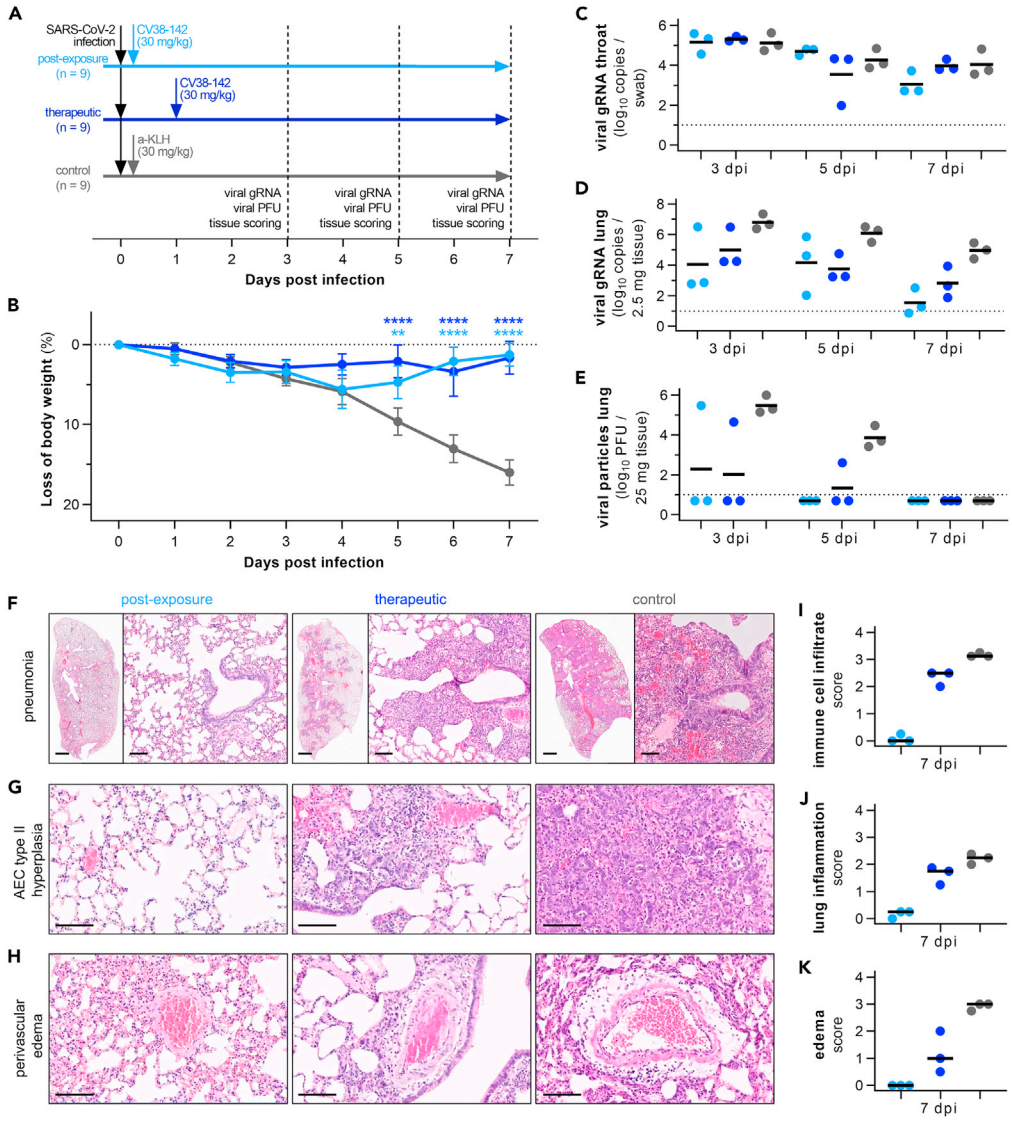

Figure 3. Efficacy in a SARS-CoV-2 VOC infection model in hamsters

(A) Schematic overview of the animal experiment. See STAR Methods for a detailed explanation of the experimental setup.

(B) Body weights of hamsters after SARS-CoV-2 VOC Alpha infection and application of SARS-CoV-2-neutralizing mAb CV38-142 at post-exposure (light blue) or therapeutic (dark blue) time point or of control mAb a-KLH (mean ± SEM from n = 9 animals per group from dpi 0 to 3, n = 6 from days 4–5; n = 3 from days 6–7; mixed-effects model with posthoc Dunnett's multiple tests in comparison to control group; significance levels shown as * ($p < 0.05$), ** ($p < 0.01$), *** ($p < 0.001$), **** ($p < 0.0001$), or not shown when not significant).

(C and D) Quantification of viral SARS-CoV-2 genomic RNA (gRNA = from (C) throat swabs or (D) homogenates of 2.5 mg lung tissue, collected at time points as indicated. RNA copies below 1 were set to 1. Bars indicate geometric mean. Dotted lines represent detection threshold.

(E) Quantification of PFU from homogenates of 25 mg lung tissue, collected at time points as indicated. Values for PFU were set to 5 when not detected. Bars indicate geometric mean. Dotted lines represent detection threshold.

(F–H) Histopathology of representative hematoxylin and eosin-stained, paraffin-embedded lung tissues at 7 dpi. Lung lobes with magnification in (F) show severe bronchointerstitial pneumonia with immune cell infiltration in the animals of the control group (right), whereas animals of the therapeutic group (center) reveal moderate signs and those of post-exposure group (left) show no signs of pneumonia. In lung parenchyma (G) signs of interstitial pneumonia with alveolar cell necrosis and type II alveolar epithelial cell hyperplasia were severe in control-treated animals (right), moderate to severe in therapeutic treatment animals (center), and absent under post-exposure conditions (right). Pulmonary blood vessels (H) in controls animals (left) revealed severe perivascular edema, perivascular lymphocytic cuffing, and alveolar

Figure 3. *Continued*
edema. In contrast, perivascular edema was moderate in therapeutic group animals (center) and absent in post-exposure group (left). Scale bars: 2000 μm in lobe overviews, 100 μm in others.
(I–K) Corresponding histopathological scores at 7 dpi are shown. Bars indicate median. See also Figure S2 and Table S2.

perivascular edema, all aspects being most pronounced at seven dpi. In contrast, the application of CV38-142 led to a noticeable reduction of these histopathological signs in the therapeutic group and to an almost complete protection of lung pathology in the post-exposure group, where bronchopulmonary changes were very mild or absent (Figures 3F–3K and Table S2). Furthermore, endothelialitis, a pathophysiological hallmark of SARS-CoV-2 infection, was also reduced in the post-exposure and therapeutic group at three dpi (Figures S2D and S2E), thereby indicating the potential of CV38-142 to protect against COVID-19 disease severity after a VOC infection.

No off-target binding in human proteome array and tissue cross-reactivity study

After confirmation of the *in vivo* efficacy of CV38-142, we completed its evaluation before the translation into the first-in-human trial by characterizing its safety profile and possible binding to non-viral off-targets. We previously mentioned that CV38-142 produced in HEK-293T cells revealed no binding to murine tissues.[1] Different glycosylation patterns due to the choice of the expression system might lead to changes in unspecific binding. We therefore repeated the experiment with CV38-142 expressed in CHO cells and again found no binding to unfixed sections of murine brain, heart, lung, liver, kidney, and colon (Figure 4A). To examine potential cross-reactivity of CV38-142 against human targets, we used two experimental approaches. Firstly, we tested for binding to approximately 6,000 native human membrane proteins in a library format of unfixed and separately transfected HEK-293T cells and by using a flow cytometry-based detection. At 20 μg/mL binding was detected as expected to the control target, the SARS-CoV-2 spike S1 protein (containing the RBD), and to the immunoglobulin gamma Fc receptor 1, but to no other human protein (Figure 4B). Secondly, we performed a tissue cross-reactivity study with 38 tissues and blood smears from three independent panels of snap-frozen human normal tissues, conducted by a certified facility in compliance with good laboratory practice (GLP) requirements. Transfected HEK-293T cells expressing SARS-CoV-2 spike S1 were used as positive control and revealed stable binding of CV38-142 over the experimental period, while the negative control of untransfected HEK-293T cells was uniformly negative (Figure 4C). In human tissues, some staining was observed in sections incubated with CV38-142 and the control mAb with identical distribution and intensity in a range of cells (granulocytes and epithelial) and tissues (containing these cells in variable amounts), where hydrophobic interactions (notably ceroid lipofuscin and/or mitochondria) or residual peroxidase activity occurred. Such findings comprise usual background staining with the used reporting system. Beyond that, importantly, no tissue cross-reactivity was observed with CV38-142 when incubated at concentrations of 0.5 μg/mL and 5 μg/mL. Thus, in conclusion, CV38-142 showed no evidence of cross-reactivity in any of the tested assays and revealed a favorable safety profile before first-in-human application.

CV38-142 does not neutralize omicron BA.1 and BA.2

Next, we aimed to characterize potency of CV38-142 against sublineages of Omicron, the VOC that had emerged while the previous experiments were conducted. No neutralizing activity was detected in authentic virus PRNT assays with Omicron BA.1 and BA.2 isolates for CV38-142 (Figures 5A and 5B). In contrast, the clinically approved mAbs sotrovimab and cilgavimab,[27,28] which bind to the same conserved RBD face as CV38-142, both neutralized BA.1 and BA.2, with sotrovimab revealing reduced potency against BA.2 (Figures 5A and 5B), similar to previous reports.[3,18] Given that CV38-142 and sotrovimab bind the SARS-CoV-2 RBD in partially overlapping epitopes and compete with each other for binding,[19] we aimed to further characterize their differences in target binding. Within the RBD of BA.1 and BA.2, there are 15 and 16 mutated residues, respectively, when compared to the wild-type RBD. Of those residues, binding of CV38-142 to wild-type RBD buries S373 and N440, whereas binding of sotrovimab buries N440, but not S373, and additionally G339 (Figure 5C and Table S3). At these sites, no direct interactions at the RBD-antibody interface have been identified for sotrovimab, but for CV38-142 at N440, which makes a hydrogen bond with Y92 of the antibodies' light chain (Table S3;[17,19]). We therefore hypothesized that the abolished neutralization of Omicron by CV38-142 could be due to Omicron's N440K substitution. However, CV38-142 bound a wild-type RBD construct with a single N440K substitution to a similar extent as the wild-type RBD but did not bind BA.1 RBD (Figure 5D). In

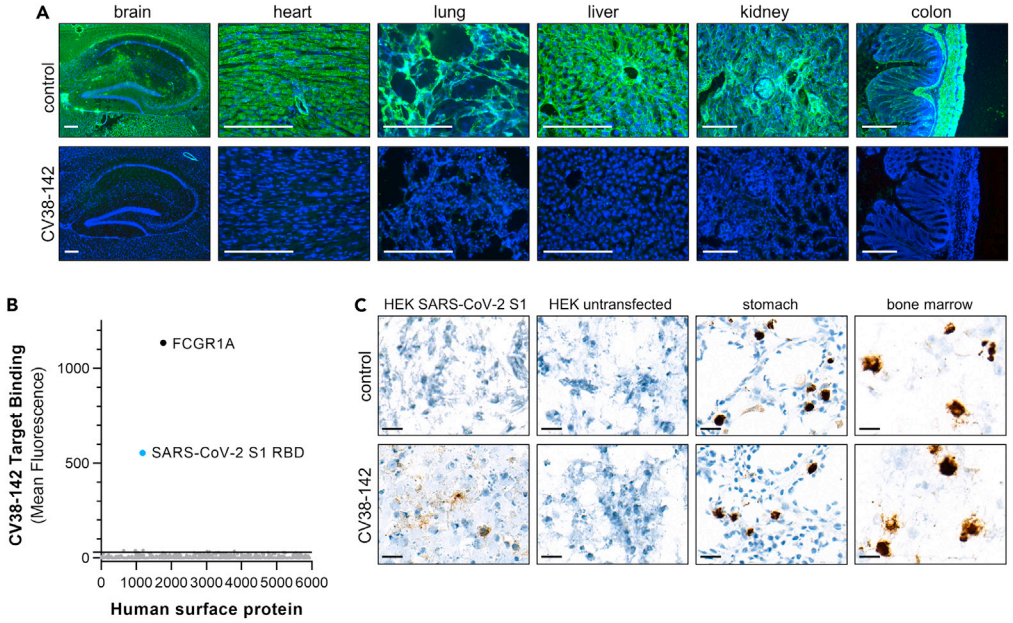

Figure 4. Off-target binding evaluation

(A) Immunofluorescence stainings of autoreactive control mAb (#011–138, upper panel) and SARS-CoV-2 mAb CV38-142 (lower panel) on unfixed sections of the indicated murine organs. mAb binding to distinct anatomical structures is shown in green, and cell nuclei are depicted in blue. Scale bars: 100 μm.

(B) Binding of CV38-142 to a library of human membrane proteins tested by flow cytometry at 20 μg/mL. Protein targets with confirmed binding interactions in downstream validation studies are displayed in blue and black, those that did not pass validation were removed. FCGR1A = Fc gamma receptor 1A.

(C) Immunohistochemical stainings of isotype-matched control mAb (upper panel) and SARS-CoV-2 mAb CV38-142 (lower panel) on HEK-293T cells either overexpressing SARS-CoV-2 S1 RBD or being untransfected or human tissues as indicated. mAb binding is shown in brown. The brown signals in granulocytes and maturing myeloid cells in the sections of stomach and bone marrow are characteristic of chromogenic staining procedures on snap-frozen tissue with residual peroxidase activities and are similarly detected with control mAb and under conditions without antibodies (reporting system only, not shown). Scale bars: 20 μm.

conclusion, CV38-142 fails to neutralize Omicron lineages BA.1 and BA.2 with the loss in neutralization likely depending on complex structural changes in the Omicron RBD.

DISCUSSION

Here, we provide the systematic selection and comprehensive preclinical characterization of the mAb CV38-142 with the intended use as a therapeutic antibody to reduce disease severity in COVID-19 patients. In contrast to antibodies that bind to the receptor-binding motif (RBM) of the SARS-CoV-2 RBD and thereby sterically block the ACE2 interaction, CV38-142 binds the RBD at a conserved epitope distant from the RBM. As the first four VOCs Alpha, Beta, Gamma, and Delta carry RBD mutations at the residues K417, L452, T478, E484, and N501, these variants affect the neutralizing activity of multiple RBM-targeting mAbs as shown for CV07-209 and CV38-183 in this study. In contrast, CV38-142 retained its broad potency against these four VOCs. However, CV38-142 revealed a loss of potency against the Omicron lineages BA.1 and BA.2, although it binds the RBD at a similar epitope as the clinically approved sotrovimab and cilgavimab, which retained neutralizing activity. We previously showed that SARS-CoV-2 binding of CV38-142 includes an interaction with N440 of the RBD.[19] Interestingly, at this position, the Omicron BA.1 and BA.2 lineages both harbor the substitution N440K, a mutation that has been shown to be part of escape variants for other mAbs of the same RBD binding class.[14] However, for CV38-142, N440K alone did not explain the loss of potency against the BA.1 and BA.2 lineages. Thus, it yet remains unclear how the neutralization of CV38-142 is affected in Omicron sublineages. The underlying mechanism may be related to complex structural changes in the Omicron RBD with marked deviations from the wild-type RBD conformation.[30] The chronology of this study demonstrates

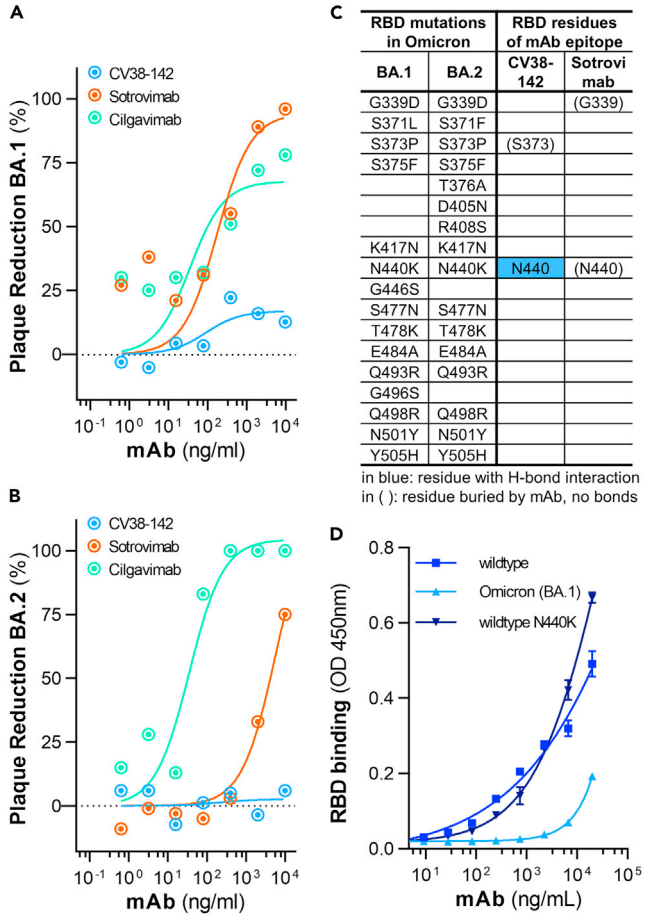

C

RBD mutations in Omicron		RBD residues of mAb epitope	
BA.1	BA.2	CV38-142	Sotrovimab
G339D	G339D		(G339)
S371L	S371F		
S373P	S373P	(S373)	
S375F	S375F		
	T376A		
	D405N		
	R408S		
K417N	K417N		
N440K	N440K	N440	(N440)
G446S			
S477N	S477N		
T478K	T478K		
E484A	E484A		
Q493R	Q493R		
G496S			
Q498R	Q498R		
N501Y	N501Y		
Y505H	Y505H		

in blue: residue with H-bond interaction
in ( ): residue buried by mAb, no bonds

Figure 5. Potency against Omicron variants BA.1 and BA.2

(A and B) Concentration-dependent neutralization of plaque formation from authentic SARS-CoV-2 Omicron isolates of (A) BA.1 or (B) BA.2 lineage by indicated mAbs. Non-linear regression models are shown. Values indicate mean from two technical duplicates.

(C) Left columns: Mutations in the SARS-COV-2 RBD of the Omicron lineages BA.1 and BA.2 relative to wild type (SARS-CoV-2 B1 lineage). Right columns: For the respective positions, epitope residues are assigned, if the buried surface area (BSA) is greater than 0 Å^2 based on the calculation by the PISA program[29] for SARS-CoV-2 RBD in complex with CV38-142[19] (PDB: 7LM8) and sotrovimab[17] (PDB: 7JX3), respectively. Residues involved in interactions as hydrogen bonds or salt bridges with RBD as identified using PISA are marked with colored background. All other RBD residues with direct involvement in the mAb epitopes are listed in Table S3.

(D) Concentration-dependent binding of mAb CV38-142 to the indicated recombinant SARS-CoV-2 RBDs as revealed by ELISA. Non-linear regression models are shown. Values indicate mean ± SD from two technical duplicates. See also Table S3.

the unpredictable characteristics of the COVID-19 pandemic, not only in terms of the incidence levels and emergences of novel variants but also with regard to the efficacy of therapeutic mAbs. The recently dominating Omicron sublineages led to the decision to discontinue the further clinical development of CV38-142 at present.

Limitations of the study

Our study shows the broad potency of CV38-142 against multiple SARS-CoV-2 variants, its therapeutic efficacy in a COVID-19 hamster model, and its favorable safety profile. However, the mAb cannot neutralize Omicron of which all currently circulating variants are descendants. While not limiting the scientific value of this study, it restricts the clinical utility of CV38-142, and there is no rationale to continue the development of CV38-142 at the moment. Given its binding to a conserved epitope

with cross-reacticity to SARS-CoV, CV38-142 may be a suitable mAb therapy candidate against future SARS-CoV-2 variants or further Coronaviridae, similar to sotrovimab that was isolated from a SARS-CoV-infected individual but clinically developed as a SARS-CoV-2 therapeutic. Moreover, our study provides guidance for systematic selection of mAb candidates and their development for clinical applications.

STAR★METHODS

Detailed methods are provided in the online version of this paper and include the following:

- KEY RESOURCES TABLE
- RESOURCE AVAILABILITY
  - Lead contact
  - Materials availability
  - Data and code availability
- EXPERIMENTAL MODEL AND SUBJECT DETAILS
  - Animal experiment approval and animal care
- METHOD DETAILS
  - Recombinant mAb production during selection process
  - Developability assessment of affinity, neutralization, SARS-CoV binding, tissue reactivity
  - Isoelectric focusing (IEF)
  - Size exclusion chromatography (SEC)
  - Nano differential scanning fluorimetry (NanoDSF)
  - Analysis for critical complementarity-determining regions (CDRs) sequence motifs
  - Bioinformatic sequence predictions
  - SARS-CoV RBD ELISA
  - Plaque reduction neutralization tests (PRNTs)
  - CHO cell line development
  - mAb production and purification from CHO cells
  - Mass spectrometric analysis
  - Surface plasmon resonance (SPR) measurements
  - SARS-CoV-2 VOC solid phase binding assays
  - Hamster model of a SARS-CoV-2 VOC infection
  - Quantification of viral RNA and functional viral particles
  - Histopathological examinations
  - Reactivity screening on murine tissues
  - Human membrane protein library screen
  - Human tissue cross-reactivity study
  - Characterization of RBD – mAb binding residues
  - RBD VOC ELISA
- QUANTIFICATION AND STATISTICAL ANALYSIS

SUPPLEMENTAL INFORMATION

Supplemental information can be found online at https://doi.org/10.1016/j.isci.2023.106323.

ACKNOWLEDGMENTS

We thank Stefanie Bandura, Matthias Sillmann, and Doreen Brandl for excellent technical assistance; Helmut Fickenscher, Corina Bahr, Miriam Schäfer, Frieda Schön, and Thomas Lorentz for their support in obtaining and characterizing suitable virus isolates; Stephan Nottelmann, Stefan Ruhland, Philipp Lang, and Kristin Schwarz for assistance with CHO cell line and mAb material generation; Marek Wieczorek and Florian Tomszak for assistance in sequence analysis and developability prediction; Jens Hellmer for analytic measurements and analyses (SEC and LCMS) as well as HyoungJin Kim, Tin Choi Lam-Schlabbach, Maximilian Posch, and Robert Schultz-Heienbrok for extensive support in preparation of the planned clinical trial. We acknowledge BIAFFIN GmbH & Co. KG (Kassel, Germany) for performing SPR measurements, Integral Molecular (Philadelphia, U.S.A.) for performing the human membrane proteome assay and TPL Path Labs GmbH (Freiburg, Germany) for performing the human tissue cross-reactivity study. J.K., S.M.R. and V.M.C. are supported by Berlin Institute of Health (BIH)-Charité Clinician Scientist program funded by Charité – Universitätsmedizin Berlin and the Berlin Institute of Health. This work was supported by the German

Research Foundation (DFG) (grants FOR3004, PR1274/3-1, and PR1274/5-1 to H.P.; project 184695641 – SFB 958, project 327654276 – SFB 1315, and under Germany's Excellence Strategy – Exc-2049-390688087 to D.S.), by the Helmholtz Association (HIL-A03 to H.P.), by the German Federal Ministry of Education and Research (Connect-Generate 01GM1908D to H.P), and by the European Research Council (ERC) under the European Union's Horizon 2020 research and innovation programme (Grant agreement No. 810580 to D.S.).

AUTHOR CONTRIBUTIONS

Conceptualization: J.K., S.M.R., U.J., and H.P.; mAb production during selection process: J.K., S.M.R., H.-C.K., and E.S.-S..; CHO cell line generation: S.E., V.N., M.M., S.K., S.H., and P.H..; Biophysical characterization: S.E., V.N., S.H., and P.H.; Virus strain isolation and neutralization testing: L.M.J., M.L.S., T.S., R.R., A.K., and V.M.C.; Hamster study: J.T., J.M.A., K.E., and A.A.; Histopathology: J.T. and S.M.; Off-target binding: J.K. and S.M.R.; Cross-reactivity to SARS-CoV RBD: H.-C.K.; Regulatory Development: J.K., S.M.R., M.M., L.E.S., U.J., and H.P.; Writing – Original Draft: J.K., S.M.R., and H.P.; Writing – Review & Editing: all authors; Visualization: J.K., S.M.R., and S.E.; Supervision: J.K., S.M.R., U.J., V.M.C., and H.P.; Funding Acquisition: J.T., D.S., and H.P.

DECLARATION OF INTERESTS

The German Center for Neurodegenerative Diseases (DZNE) and Charité-Universitätsmedizin Berlin have filed a patent application (application number: PCT/EP2021/064,352) on antibodies for the treatment of SARS-CoV-2 infection on which J.K., S.M.R., H.-C.K., E.S.-S., L.E.S., V.M.C., and H.P. are named as inventors. V.M.C. is named together with Euroimmun GmbH on a patent application filed recently regarding the diagnostic of SARS-CoV-2 by antibody testing. S.E., V.N., M.M., S.K., S.H., P.H., and U.J. are employees of Miltenyi Biotec B.V. & Co. KG.

INCLUSION AND DIVERSITY

We support inclusive, diverse, and equitable conduct of research.

Received: August 8, 2022
Revised: December 15, 2022
Accepted: February 22, 2023
Published: March 2, 2023

REFERENCES

1. Kreye, J., Reincke, S.M., Kornau, H.C., Sánchez-Sendin, E., Corman, V.M., Liu, H., Yuan, M., Wu, N.C., Zhu, X., Lee, C.C.D., et al. (2020). A therapeutic non-self-reactive SARS-CoV-2 antibody protects from lung pathology in a COVID-19 hamster model. Cell *183*, 1058–1069.e19. https://doi.org/10.1016/j.cell.2020.09.049.

2. Ulrich, L., Halwe, N.J., Taddeo, A., Ebert, N., Schön, J., Devisme, C., Trüeb, B.S., Hoffmann, B., Wider, M., Fan, X., et al. (2022). Enhanced fitness of SARS-CoV-2 variant of concern Alpha but not Beta. Nature *602*, 307–313. https://doi.org/10.1038/s41586-021-04342-0.

3. Cameroni, E., Bowen, J.E., Rosen, L.E., Saliba, C., Zepeda, S.K., Culap, K., Pinto, D., VanBlargan, L.A., De Marco, A., di Iulio, J., et al. (2022). Broadly neutralizing antibodies overcome SARS-CoV-2 Omicron antigenic shift. Nature *602*, 664–670. https://doi.org/10.1038/s41586-021-04386-2.

4. Lucas, C., Vogels, C.B.F., Yildirim, I., Rothman, J.E., Lu, P., Monteiro, V., Gehlhausen, J.R., Campbell, M., Silva, J., Tabachnikova, A., et al. (2021). Impact of circulating SARS-CoV-2 variants on mRNA vaccine-induced immunity. Nature *600*, 523–529. https://doi.org/10.1038/s41586-021-04085-y.

5. Planas, D., Saunders, N., Maes, P., Guivel-Benhassine, F., Planchais, C., Buchrieser, J., Bolland, W.H., Porrot, F., Staropoli, I., Lemoine, F., et al. (2022). Considerable escape of SARS-CoV-2 Omicron to antibody neutralization. Nature *602*, 671–675. https://doi.org/10.1038/s41586-021-04389-z.

6. Gruell, H., Vanshylla, K., Tober-Lau, P., Hillus, D., Schommers, P., Lehmann, C., Kurth, F., Sander, L.E., and Klein, F. (2022). mRNA booster immunization elicits potent neutralizing serum activity against the SARS-CoV-2 Omicron variant. Nat. Med. *28*, 477–480. https://doi.org/10.1038/s41591-021-01676-0.

7. Rössler, A., Riepler, L., Bante, D., von Laer, D., and Kimpel, J. (2022). SARS-CoV-2 Omicron variant neutralization in serum from vaccinated and convalescent persons. N. Engl. J. Med. *386*, 698–700. https://doi.org/10.1056/NEJMc2119236.

8. Troiano, G., and Nardi, A. (2021). Vaccine hesitancy in the era of COVID-19. Publ. Health *194*, 245–251. https://doi.org/10.1016/j.puhe.2021.02.025.

9. Lee, A., Wong, S.Y., Chai, L.Y.A., Lee, S.C., Lee, M.X., Muthiah, M.D., Tay, S.H., Teo, C.B., Tan, B.K.J., Chan, Y.H., et al. (2022). Efficacy of covid-19 vaccines in immunocompromised patients: systematic review and meta-analysis. BMJ *376*, e068632. https://doi.org/10.1136/bmj-2021-068632.

10. Weinreich, D.M., Sivapalasingam, S., Norton, T., Ali, S., Gao, H., Bhore, R., Musser, B.J., Soo, Y., Rofail, D., Im, J., et al. (2021). REGN-COV2, a neutralizing antibody cocktail, in outpatients with covid-19. N. Engl. J. Med. *384*, 238–251. https://doi.org/10.1056/NEJMoa2035002.

11. Gupta, A., Gonzalez-Rojas, Y., Juarez, E., Crespo Casal, M., Moya, J., Falci, D.R., Sarkis, E., Solis, J., Zheng, H., Scott, N., et al. (2021). Early treatment for covid-19 with SARS-CoV-2 neutralizing antibody Sotrovimab. N. Engl. J. Med. *385*, 1941–1950. https://doi.org/10.1056/NEJMoa2107934.

12. Ku, Z., Xie, X., Hinton, P.R., Liu, X., Ye, X., Muruato, A.E., Ng, D.C., Biswas, S., Zou, J., Liu, Y., et al. (2021). Nasal delivery of an IgM

offers broad protection from SARS-CoV-2 variants. Nature *595*, 718–723. https://doi.org/10.1038/s41586-021-03673-2.

13. Li, C., Zhan, W., Yang, Z., Tu, C., Hu, G., Zhang, X., Song, W., Du, S., Zhu, Y., Huang, K., et al. (2022). Broad neutralization of SARS-CoV-2 variants by an inhalable bispecific single-domain antibody. Cell *185*, 1389–1401.e18. https://doi.org/10.1016/j.cell.2022.03.009.

14. Cao, Y., Wang, J., Jian, F., Xiao, T., Song, W., Yisimayi, A., Huang, W., Li, Q., Wang, P., An, R., et al. (2022). Omicron escapes the majority of existing SARS-CoV-2 neutralizing antibodies. Nature *602*, 657–663. https://doi.org/10.1038/s41586-021-04385-3.

15. Hoffmann, M., Krüger, N., Schulz, S., Cossmann, A., Rocha, C., Kempf, A., Nehlmeier, I., Graichen, L., Moldenhauer, A.S., Winkler, M.S., et al. (2022). The Omicron variant is highly resistant against antibody-mediated neutralization: implications for control of the COVID-19 pandemic. Cell *185*, 447–456.e11. https://doi.org/10.1016/j.cell.2021.12.032.

16. Pinto, D., Park, Y.J., Beltramello, M., Walls, A.C., Tortorici, M.A., Bianchi, S., Jaconi, S., Culap, K., Zatta, F., De Marco, A., et al. (2020). Cross-neutralization of SARS-CoV-2 by a human monoclonal SARS-CoV antibody. Nature *583*, 290–295. https://doi.org/10.1038/s41586-020-2349-y.

17. Piccoli, L., Park, Y.J., Tortorici, M.A., Czudnochowski, N., Walls, A.C., Beltramello, M., Silacci-Fregni, C., Pinto, D., Rosen, L.E., Bowen, J.E., et al. (2020). Mapping neutralizing and immunodominant sites on the SARS-CoV-2 spike receptor-binding domain by structure-guided high-resolution serology. Cell *183*, 1024–1042.e21. https://doi.org/10.1016/j.cell.2020.09.037.

18. Iketani, S., Liu, L., Guo, Y., Liu, L., Chan, J.F.W., Huang, Y., Wang, M., Luo, Y., Yu, J., Chu, H., et al. (2022). Antibody evasion properties of SARS-CoV-2 Omicron sublineages. Nature *604*, 553–556. https://doi.org/10.1038/s41586-022-04594-4.

19. Liu, H., Yuan, M., Huang, D., Bangaru, S., Zhao, F., Lee, C.C.D., Peng, L., Barman, S., Zhu, X., Nemazee, D., et al. (2021). A combination of cross-neutralizing antibodies synergizes to prevent SARS-CoV-2 and SARS-CoV pseudovirus infection. Cell Host Microbe *29*, 806–818.e6. https://doi.org/10.1016/j.chom.2021.04.005.

20. Reincke, S.M., Yuan, M., Kornau, H.C., Corman, V.M., van Hoof, S., Sánchez-Sendin, E., Ramberger, M., Yu, W., Hua, Y., Tien, H., et al. (2022). SARS-CoV-2 Beta variant infection elicits potent lineage-specific and cross-reactive antibodies. Science *375*, 782–787. https://doi.org/10.1126/science.abm5835.

21. Brouwer, P.J.M., Caniels, T.G., van der Straten, K., Snitselaar, J.L., Aldon, Y., Bangaru, S., Torres, J.L., Okba, N.M.A., Claireaux, M., Kerster, G., et al. (2020). Potent neutralizing antibodies from COVID-19 patients define multiple targets of vulnerability. Science *369*, 643–650. https://doi.org/10.1126/science.abc5902.

22. Rogers, T.F., Zhao, F., Huang, D., Beutler, N., Burns, A., He, W.T., Limbo, O., Smith, C., Song, G., Woehl, J., et al. (2020). Isolation of potent SARS-CoV-2 neutralizing antibodies and protection from disease in a small animal model. Science *369*, 956–963. https://doi.org/10.1126/science.abc7520.

23. Rockx, B., Corti, D., Donaldson, E., Sheahan, T., Stadler, K., Lanzavecchia, A., and Baric, R. (2008). Structural basis for potent cross-neutralizing human monoclonal antibody protection against lethal human and zoonotic severe acute respiratory syndrome coronavirus challenge. J. Virol. *82*, 3220–3235. https://doi.org/10.1128/JVI.02377-07.

24. Nouailles, G., Wyler, E., Pennitz, P., Postmus, D., Vladimirova, D., Kazmierski, J., Pott, F., Dietert, K., Muelleder, M., Farztdinov, V., et al. (2021). Temporal omics analysis in Syrian hamsters unravel cellular effector responses to moderate COVID-19. Nat. Commun. *12*, 4869. https://doi.org/10.1038/s41467-021-25030-7.

25. Wyler, E., Adler, J.M., Eschke, K., Teixeira Alves, G., Peidli, S., Pott, F., Kazmierski, J., Michalick, L., Kershaw, O., Bushe, J., et al. (2022). Key benefits of dexamethasone and antibody treatment in COVID-19 hamster models revealed by single-cell transcriptomics. Mol. Ther. *30*, 1952–1965. https://doi.org/10.1016/j.ymthe.2022.03.014.

26. Osterrieder, N., Bertzbach, L.D., Dietert, K., Abdelgawad, A., Vladimirova, D., Kunec, D., Hoffmann, D., Beer, M., Gruber, A.D., and Trimpert, J. (2020). Age-dependent progression of SARS-CoV-2 infection in Syrian hamsters. Viruses *12*. https://doi.org/10.3390/v12070779.

27. Zost, S.J., Gilchuk, P., Chen, R.E., Case, J.B., Reidy, J.X., Trivette, A., Nargi, R.S., Sutton, R.E., Suryadevara, N., Chen, E.C., et al. (2020). Rapid isolation and profiling of a diverse panel of human monoclonal antibodies targeting the SARS-CoV-2 spike protein. Nat. Med. *26*, 1422–1427. https://doi.org/10.1038/s41591-020-0998-x.

28. Dong, J., Zost, S.J., Greaney, A.J., Starr, T.N., Dingens, A.S., Chen, E.C., Chen, R.E., Case, J.B., Sutton, R.E., Gilchuk, P., et al. (2021). Genetic and structural basis for SARS-CoV-2 variant neutralization by a two-antibody cocktail. Nat. Microbiol. *6*, 1233–1244. https://doi.org/10.1038/s41564-021-00972-2.

29. Krissinel, E., and Henrick, K. (2007). Inference of macromolecular assemblies from crystalline state. J. Mol. Biol. *372*, 774–797. https://doi.org/10.1016/j.jmb.2007.05.022.

30. McCallum, M., Czudnochowski, N., Rosen, L.E., Zepeda, S.K., Bowen, J.E., Walls, A.C., Hauser, K., Joshi, A., Stewart, C., Dillen, J.R., et al. (2022). Structural basis of SARS-CoV-2 Omicron immune evasion and receptor engagement. Science *375*, 864–868. https://doi.org/10.1126/science.abn8652.

31. Kreye, J., Wenke, N.K., Chayka, M., Leubner, J., Murugan, R., Maier, N., Jurek, B., Ly, L.T., Brandl, D., Rost, B.R., et al. (2016). Human cerebrospinal fluid monoclonal N-methyl-D-aspartate receptor autoantibodies are sufficient for encephalitis pathogenesis. Brain *139*, 2641–2652. https://doi.org/10.1093/brain/aww208.

32. Wölfel, R., Corman, V.M., Guggemos, W., Seilmaier, M., Zange, S., Müller, M.A., Niemeyer, D., Jones, T.C., Vollmar, P., Rothe, C., et al. (2020). Virological assessment of hospitalized patients with COVID-2019. Nature *581*, 465–469. https://doi.org/10.1038/s41586-020-2196-x.

33. Niemeyer, D., Stenzel, S., Veith, T., Schroeder, S., Friedmann, K., Weege, F., Trimpert, J., Heinze, J., Richter, A., Jansen, J., et al. (2022). SARS-CoV-2 variant Alpha has a spike-dependent replication advantage over the ancestral B.1 strain in human cells with low ACE2 expression. PLoS Biol. *20*, e3001871. https://doi.org/10.1371/journal.pbio.3001871.

34. Rose, R., Neumann, F., Müller, S., Bäumler, C., Schäfer, M., Schön, F., Römpke, J., Schulze, S., Weyer, D., Grobe, O., et al. (2022). Delta or Omicron BA.1/2-neutralizing antibody levels and T-cell reactivity after triple-vaccination or infection. Allergy *77*, 3130–3133. https://doi.org/10.1111/all.15395.

35. Corman, V.M., Landt, O., Kaiser, M., Molenkamp, R., Meijer, A., Chu, D.K., Bleicker, T., Brünink, S., Schneider, J., Schmidt, M.L., et al. (2020). Detection of 2019 novel coronavirus (2019-nCoV) by real-time RT-PCR. Euro Surveill. *25*. https://doi.org/10.2807/1560-7917.ES.2020.25.3.2000045.

36. Swindells, M.B., Porter, C.T., Couch, M., Hurst, J., Abhinandan, K.R., Nielsen, J.H., Macindoe, G., Hetherington, J., and Martin, A.C.R. (2017). abYsis: integrated antibody sequence and structure-management, analysis, and prediction. J. Mol. Biol. *429*, 356–364. https://doi.org/10.1016/j.jmb.2016.08.019.

37. Raybould, M.I.J., Marks, C., Krawczyk, K., Taddese, B., Nowak, J., Lewis, A.P., Bujotzek, A., Shi, J., and Deane, C.M. (2019). Five computational developability guidelines for therapeutic antibody profiling. Proc. Natl. Acad. Sci. USA *116*, 4025–4030. https://doi.org/10.1073/pnas.1810576116.

38. Conchillo-Solé, O., de Groot, N.S., Avilés, F.X., Vendrell, J., Daura, X., and Ventura, S. (2007). AGGRESCAN: a server for the prediction and evaluation of "hot spots" of aggregation in polypeptides. BMC Bioinf. *8*, 65. https://doi.org/10.1186/1471-2105-8-65.

39. Hebditch, M., Carballo-Amador, M.A., Charonis, S., Curtis, R., and Warwicker, J. (2017). Protein-Sol: a web tool for predicting protein solubility from sequence. Bioinformatics *33*, 3098–3100. https://doi.org/10.1093/bioinformatics/btx345.

40. Reincke, S.M., Prüss, H., and Kreye, J. (2020). Brain antibody sequence evaluation (BASE): an easy-to-use software for complete data analysis in single cell immunoglobulin cloning. BMC Bioinf. *21*, 446. https://doi.org/10.1186/s12859-020-03741-w.

41. Kreye, J., Wright, S.K., van Casteren, A., Stöffler, L., Machule, M.L., Reincke, S.M., Nikolaus, M., van Hoof, S., Sanchez-Sendin, E., Homeyer, M.A., et al. (2021). Encephalitis patient-derived monoclonal GABAA receptor antibodies cause epileptic seizures. J. Exp. Med. *218*, e20210012. https://doi.org/10.1084/jem.20210012.

42. Nakamura, T., Karakida, N., Dantsuka, A., Ichii, O., Elewa, Y.H.A., Kon, Y., Nagasaki, K.I., Hattori, H., and Yoshiyasu, T. (2017). Effects of a mixture of medetomidine, midazolam and butorphanol on anesthesia and blood biochemistry and the antagonizing action of atipamezole in hamsters. J. Vet. Med. Sci. *79*, 1230–1235. https://doi.org/10.1292/jvms.17-0210.

43. Zivcec, M., Safronetz, D., Haddock, E., Feldmann, H., and Ebihara, H. (2011). Validation of assays to monitor immune responses in the Syrian golden hamster (Mesocricetus auratus). J. Immunol. Methods *368*, 24–35. https://doi.org/10.1016/j.jim.2011.02.004.

44. Dietert, K., Gutbier, B., Wienhold, S.M., Reppe, K., Jiang, X., Yao, L., Chaput, C., Naujoks, J., Brack, M., Kupke, A., et al. (2017). Spectrum of pathogen- and model-specific histopathologies in mouse models of acute pneumonia. PLoS One *12*, e0188251. https://doi.org/10.1371/journal.pone.0188251.

45. Tucker, D.F., Sullivan, J.T., Mattia, K.A., Fisher, C.R., Barnes, T., Mabila, M.N., Wilf, R., Sulli, C., Pitts, M., Payne, R.J., et al. (2018). Isolation of state-dependent monoclonal antibodies against the 12-transmembrane domain glucose transporter 4 using virus-like particles. Proc. Natl. Acad. Sci. USA *115*, E4990–E4999. https://doi.org/10.1073/pnas.1716788115.

STAR★METHODS

KEY RESOURCES TABLE

REAGENT or RESOURCE	SOURCE	IDENTIFIER
Antibodies		
donkey anti-rabbit IgG	Dianova	Cat# 711-005-152; RRID:AB_2340585
donkey anti-human IgG, HRP-conjugated	Dianova	Cat# 709-035-149; RRID:AB_2340495
Anti-CHO (clone HA3.21E5.6)	Miltenyi Biotec	N/A
Anti-hIgG (Fd specific) (clone HP6045)	Merck	Cat# MAB1304; RRID:AB_94106
Anti-hIgG1-APC (clone IS11-12E4.23.20)	Miltenyi Biotec	Cat# 130-119-857; RRID:AB_2751893
Anti-Lambda-PE (clone IS7-24C)	Miltenyi Biotec	Cat# 130-119-778; RRID:AB_2751837
Anti-light-kappa-PE (clone IS11-24D5)	Miltenyi Biotec	Cat# 130-123-246; RRID:AB_2802012
Anti-Biotin (clone Bio3-18E7)	Miltenyi Biotec	N/A
anti-His (clone GG11-6F4.3.2)	Miltenyi Biotec	Cat# 130-092-785; RRID:AB_1103231
Anti-Fc-HRP	Sigma	Cat# A0170; RRID:AB_257868
mouse anti-human IgG (MT145)	Mabtech	Cat# 3850-1-250; RRID:AB_10697677
Mouse anti-human IgG mAb, ALP-conjugated (MT78)	Mabtech	Cat# 3850-9A; RRID:AB_10697678
goat-anti human IgG-Alexa Fluor 488	Dianova	Cat# 109-545-088; RRID:AB_2337838
goat anti-human IgG-Alexa Fluor 488	Dianova	Cat# 109-545-003; RRID:AB_2337831
a-KLH	Miltenyi Biotec	N/A
011-138	Kreye et al., 2016[31]	N/A
I5154	Sigma	Cat# I5154; RRID:AB_1163610
Bacterial and virus strains		
SARS-CoV-2 wildtype strain (Munich isolate 984)	Wölfel et al., 2020[32]	BetaCoV/Germany/BavPat1/2020
SARS-CoV-2 VOC Alpha	Niemeyer et al., 2022[33]	GISAID accession no EPI_ISL_802995
SARS-CoV-2 VOC Beta	Niemeyer et al., 2022[33]	GISAID accession no EPI_ISL_862149
SARS-CoV-2 VOC Gamma	VOC Gamma kindly provided by Dr. Chantal Reusken	https://www.european-virus-archive.com/ Ref-SKU: 014V-04089
SARS-CoV-2 VOC Delta	Niemeyer et al., 2022[33]	GISAID accession no EPI_ISL_2500366
SARS-CoV-2 VOC Omicron BA.1	Rose et al., 2022[34]	GISAID accession no EPI_ISL_7019047
SARS-CoV-2 VOC Omicron BA.2	This paper	GISAID accession no EPI_ISL_9553935
SARS-CoV2 VOC Alpha (hamster study)	Niemeyer et al., 2022[33]	BetaCoV/Germany/ChVir21652/2020, GISAID accession ID EPI_ISL_802995
Biological samples		
Hamster lungs, swabs, nasal washes	This paper	N/A
Chemicals, peptides, and recombinant proteins		
DMEM, high glucose, GlutaMAX Supplement, pyruvate	Life Technologies	Cat#31966-047
MEM non-essential amino acid solution (100x)	Sigma Aldrich	Cat#M7145
Fetal Bovine Serum	Sigma Aldrich	Cat#F7524
0,05% Trypsin EDTA phenol red	Life Technologies	Cat#25300-054
Penicillin-Streptomycin	Sigma Aldrich	Cat#P0781
Polyethylenimine, branched	Sigma Aldrich	Cat#408727
Protein G Sepharose 4 Fast flow	GE Healthcare	Cat#17-0618-01
Albumin Fraktion V Powder, protease free	Carl Roth	Cat#T844.2
Bovine Serum Albumin (IgG-free, Protease-free)	Dianova	Cat#001-000-161
StartingBlock (PBS) Blocking Buffer	Thermo Fisher	Cat#37538

(*Continued on next page*)

Continued

REAGENT or RESOURCE	SOURCE	IDENTIFIER
Tween 20	Applichem	Cat#A4974
Opti-Pro serumfree medium	Gibco	Cat# 12309050
1-step Ultra TMB-ELISA	Thermo Fisher	Cat#34028
1-step Slow TMB-ELISA	Thermo Fisher	Cat#34024
Streptavidin-POD conjugate	Roche Diagnostics	Cat#11089153001
SARS-CoV-2 S protein-RBD-mFC	Acrobiosystems	Cat# SPD-C5259
Biotinylated Human ACE2	Acrobiosystems	Cat# AC2-H82E6
SARS-CoV-2 S protein RBD, His Tag	Acrobiosystems	Cat# SPD-C52H3
Sodium chloride (NaCl)	Sigma-Aldrich	Cat#S9888
Tris Base	Sigma-Aldrich	Cat#11814273001
Concentrated hydrochloric acid (HCl)	Sigma-Aldrich	Cat#H1758
Phosphate-buffered saline (PBS)	Thermo Fisher	Cat#14040133
Normal Goat Serum	Abcam	Cat#ab138478
Paraformaldehyd	Alfa Aesar	Cat#J61899
Roti®-Mount Fluor-Care DAPI	Carl Roth	Cat#HP20.1
100x HT supplement	Gibco	Cat# 11067-030
1 M HEPES	Lonza	Cat# 17-737E
Acetic Acid	Merck	Cat# 1000632511
ProCHO™ 5 medium	Lonza	Cat# BELN12-766Q
L-Glutamin, 200 mM	Lonza	Cat# BE-17-605E
Di-sodium carbonate (Na_2CO_3)	Merck	Cat# 106392
Sodium hydrogen carbonate ($NaHCO_3$)	Merck	Cat# 106329
Trizma Base	Sigma Aldrich	Cat# T1503-5KG
MACS GMP PBS/$MgCl_2$ buffer	Miltenyi Biotec	Cat# 170-076-155
MACS GMP Tytonase (20x)	Miltenyi Biotec	Cat# 170-076-210
Human serum albumin (25%)	Octapharma	Cat# NDC68982-643-02
Sodium hydroxide pellets (NaOH)	Merck	Cat# 1.06482.1000
Citric acid monohydrate	Merck	Cat# 1.00244.1000
30% BSA	Sigma	Cat# A7284
Recombinant SARS-CoV-2 RBD (HEK)	Miltenyi Biotec	Cat# 130-127-457
Recombinant SARS-CoV-2 RBD B.1.617.2 (HEK)	Miltenyi Biotec	Cat# 130-129-703
Recombinant SARS-CoV-2 RBD B.1.1.7 (HEK)	Miltenyi Biotec	Cat# 130-128-479
Recombinant SARS-CoV-2 RBD B.1.351 (HEK)	Miltenyi Biotec	Cat# 130-128-930
Novex™ pH 3–10 IEF Protein Gels	Invitrogen	Cat# EC6655BOX
KPL Wash Solution (20x)	Seracare	Cat# 5150-0008
H_3PO_4	NeoFroxx	Cat# 5AB8F05C
DTT	Roth	Cat# 6908.2
TMB ELISA substrate	Serva	Cat# 37068.01
PD-10 desalting columns	Cytiva	Cat# 52-1308-00
IgG ELISA Kit	Invitrogen	Cat# 88-50550-88
HiTrap™ MabSelect™	Cytiva	Cat# 28408256
MACSQuant® Tyto® Cartridges	Miltenyi Biotec	Cat# 130-104-791
PNGase F	Promega	Cat# V4831
OCT medium (Roth).	Roth	Cat# 6478.1
Ventana diluent	Ventana	Cat# 760-108

(*Continued on next page*)

Continued

REAGENT or RESOURCE	SOURCE	IDENTIFIER
DAB Map detection system	Ventana	Cat# 760-124
Hematoxylin II	Ventana	Cat# 790-2208
Bluing reagent	Ventana	Cat# 760-2037
SARS-CoV-2 (COVID-19) S protein RBD (N440K)	Acrobiosystems	Cat# SRD-C52H2
Critical commercial assays		
SeraSpot® Anti-SARS-CoV-2 IgG	Seramun Diagnostica GmbH	N/A
innuPrep Virus DNA/RNA Kit	Analytic Jena	Cat#845-KS-4700250
Luna Universal Probe One-Step RT-qPCR kit	New England Biolabs	Cat#E3006L
Membrane Proteome Array	Integral Molecular	N/A
Human IgG ELISA development kit (ALP)	Mabtech	Cat#3850-1AD-6
AdvanceBio SEC 300A column	Agilent	N/A
EZ-Link™ NHS-LC-LC Biotin (Pierce)	Pierce	Cat# 21343
Deposited data		
Nucleotide sequences of antibodies shown in Figure 1	Kreye et al., 2020[1]	Genbank accession numbers MW002770 – MW002805
Experimental models: Cell lines		
HEK293-T cells	DSMZ	Cat#ACC 635
CHO DG44 cells	Invitrogen	Cat# 12613014
VeroE6 cells	ATCC	Cat#CRL-1586
Experimental models: Organisms/strains		
Syrian hamster, *Mesocricetus auratus*	Janvier	RjHan:Aura
Oligonucleotides		
SARS-CoV-2 RT-qPCR primers and probe	Corman et al., 2020[35]	N/A
SARS-CoV-2 sgRNA RT-qPCR primers and probe	Wölfel et al., 2020[32]	N/A
Recombinant DNA		
Plasmid for expression of rabbit Fc-tagged SARS-CoV-2 RBD	Kreye et al., 2020[1]	N/A
Plasmid for expression of rabbit Fc-tagged SARS-CoV RBD	Kreye et al., 2020[1]	N/A
Software and algorithms		
Biacore T200 Version 3.2	Cytiva	https://www.cytivalifesciences.com
Microsoft Excel, Word, PowerPoint	Microsoft Office	https://www.microsoft.com
GraphPad Prism, Version 8/9	GraphPad Software	https://www.graphpad.com
Biorender	BioRender	https://biorender.com
abYsis 3.4.1	Swindells et al., 2017[36]	N/A
Therapeutic Antibody Profiler	Raybould et al., 2019[37]	http://opig.stats.ox.ac.uk/webapps/newabdab/sabpred/tap
AGGRESCAN	Conchillo-Sole et al., 2007[38]	http://bioinf.uab.es/aggrescan/
Protein-Sol	Hebditch et al., 2017[39]	https://protein-sol.manchester.ac.uk/
FlowLogic, Version 7.2.1	Invai Technologies	https://www.inivai.com/flologic
MACSQuantifyTM, 2.13.0	Miltenyi Biotec	Cat# 130-094-556
Other		
1260 Infinity II HPLC	Agilent	N/A
Tycho NT.6	NanoTemper Technologies	N/A

RESOURCE AVAILABILITY

Lead contact

Further information and requests for resources and reagents should be directed to and will be fulfilled by the lead contact, Jakob Kreye (jakob.kreye@dzne.de).

Materials availability

All requests for materials including mAbs, viruses, plasmids and proteins generated in this study should be directed to the lead contact author. Materials will be made available under a Material Transfer Agreement (MTA) for non-commercial usage.

Data and code availability

Sequence information for the mAbs described in this study can be found in original publication in which they had been isolated.[1] The custom software BASE used for immunoglobulin sequence analysis is available at https://github.com/automatedSequencing/BASE. The nucleotide sequences of all mAbs shown in Figure 1 have been deposited to GenBank (accession numbers MW002770 – MW002805).

EXPERIMENTAL MODEL AND SUBJECT DETAILS

Animal experiment approval and animal care

The animal experiment was approved by the Landesamt für Gesundheit und Soziales in Berlin, Germany (approval number 0086/20) and performed in compliance with relevant national and international guidelines for care and humane use of animals. *In vitro* and animal work was conducted under appropriate biosafety precautions in a BSL-3 facility at the Institute of Virology, Freie Universität Berlin, Germany. Twenty-seven six week old female and male golden Syrian hamsters (*Mesocricetus auratus*; outbred hamster strain RjHan:AURA, Janvier Labs) were kept in groups of 1–3 animals in enriched, individually ventilated cages (GR-900, Tecniplast). The animals had *ad libitum* access to food and water and were allowed to acclimate to these conditions for seven days prior to viral infection. Cage temperatures and relative humidity were recorded daily and ranged from 22 – 24°C and 40%–55%, respectively.

METHOD DETAILS

Recombinant mAb production during selection process

All mAbs described in Figure 1 have been isolated in a previous study.[1] For the selection of lead candidates for CHO cell line generation and further development, mAbs were generated by transient transfection as previously described. In brief, stored expression vectors were sequenced to confirm sequence identify using cBASE module of our costum immunoglobulin (Ig) sequence analysis software BASE.[40] Human embryonic kidney cells (HEK-293T) were transiently transfected with pairs of Ig heavy and light chain vectors, mAb containing cell culture supernatant was harvested, mAbs purified using Protein G Sepharose beads (GE Healthcare) and Ig concentration determined using a commercial ELISA kit (Mabtech), all following established protocols.[1,31,41]

Developability assessment of affinity, neutralization, SARS-CoV binding, tissue reactivity

The prediction of the potential mAb developability included functional parameters that have been previously acquired.[1] Regarding SARS-CoV-2 RBD affinity, K_D-values were considered favorable when below 1.0 E−11 M, or unfavorable when above 1.0 E−8 M or neutral when in between. Regarding SARS-CoV-2 neutralization, the half-maximal inhibitory concentration (IC_{50}) when using authentic SARS-CoV-2 wildtype isolate were considered favorable when below 5 ng/ml, or unfavorable when above 50 ng/ml or neutral when in between. SARS-CoV binding was previously tested with mAb concentration at 1 μg/ml and here considered favorable if binding was detected or neutral if binding was not detected. Murine tissue reactivity was previously tested using unfixed sections of brain, lung, heart, liver, colon and kidney with mAb concentration at 5 μg/ml and were considered favorable if no binding was detected or unfavorable if binding was detected.

Isoelectric focusing (IEF)

To evaluate possible limitation factors for mAb product formulation and application, the isoelectric point (pI) of each mAb as a marker for critical pH conditions that may lead to protein aggregation was determined by isoelectric focusing (IEF) using Novex™ pH 3–10 IEF protein gels (Invitrogen) according to the

manufacturer's instructions. Gels were then stained with Coomassie Brilliant Blue. IEF Marker 3–10 (SERVA Electrophoresis GmbH) served as protein marker. pI values greater than 7.8 were considered as favorable.

Size exclusion chromatography (SEC)

To evaluate to aggregation behavior, size exclusion chromatography was conducted on a 1260 Infinity II HPLC (Agilent) using an AdvanceBio SEC 300A column (Agilent). A linear PBS gradient was used for separation. Molecular weights were calibrated using a molecular weight gel filtration standard (Biorad), according to the supplier's instructions. The monomer content was quantified to evaluate the level of aggregation and was calculated as the ratio of the monomer containing peak area to total mAb peak areas. Monomer contents were considered favorable when greater than 99%, or unfavorable when below 96% or neutral when in between.

Nano differential scanning fluorimetry (NanoDSF)

To evaluate their structural stability, folding state and structural integrity of purified mAbs were analyzed by intrinsic fluorescence changes using the Tycho NT.6 (NanoTemper Technologies). Each sample was loaded into capillary tubes and a linear thermal ramp (30°C/minute from 35°C to 95°C) was applied. Unfolding transition points as indicator for the structural stability of the proteins were determined from changes in the emission wavelengths of tryptophan fluorescence at 350 and 330 nm according to the manufacturer's instructions. Inflection temperatures representing CH2, CH3 and Fab domain (if present as peak) were analyzed. Values were considered favorable when greater than 73°C (CH2), 75°C (Fab) and 83°C (CH3) respectively; or unfavorable when below $\leq$68°C (CH2), 70°C (Fab) and 75°C (CH3) respectively. Initial ratios as measure of mAb stability before heating were considered favorable when below 0.7, or unfavorable when above $\geq$0.9 or neutral when in between.

Analysis for critical complementarity-determining regions (CDRs) sequence motifs

For sequence motif analysis in CDRs (Kabat numbering scheme) the web-based tool abYsis in version 3.4.1 was used[36] (www.abysis.org). Cysteine residues and N-glycosylation motifs (NxS/T) in CDRs were considered as unfavorable and regarded as criterion for exclusion. The following motifs in CDRs may be potential risk factors for developability and were considered as neutral when occurring at low frequency: methionine as oxidation-prone residue, the most common deamidation motifs (NG, NS, NN, NT and NA) and typical aspartate isomerization sites, especially DG. If none of these motifs were present in heavy or light chain CDRs, they were considered as favorable.

Bioinformatic sequence predictions

The mAb sequences were analyzed *in silico* to assign potential risk factors that affect the developability of the respective mAb proteins. The evaluation included an analysis with the Therapeutic Antibody Profiler (TAP) prediction tool[37] to predict (i) the total length of CDRs, (ii) the extent of hydrophobicity as measured by patches of surface hydrophobicity (PSH), (iii) the regions of dense charge as measured by number of patches of positive charge (PPC) or (iv) negative charge (PNC) and (v) the asymmetry in the net heavy and light chain surface charge as measured by the structural Fv charge symmetry parameter (SFvCSP). In addition, we used the web-based tools AGGRESACAN to predict aggregation-prone regions[38] and Protein-Sol to calculate protein solubility from sequence.[39] Results from all software tools were considered for scoring. TAP score was taken into account with 80%, AGGRESACAN with 15% and Protein-Sol with 5%.

SARS-CoV RBD ELISA

An RBD-Fc ELISA was used to determine mAb reactivity as described previously.[1] Briefly, RBD-Fc fusion proteins containing the RBD-SD1 regions of the spike S1 subunit of SARS-CoV (amino acids 306–577) or SARS-CoV-2 (amino acids 319–591) and the Fc region of rabbit IgG were expressed in HEK-293T cells and immobilized onto 96-well plates via anti-rabbit IgG (Dianova, 711-005-152). Binding of human mAbs was detected using horseradish peroxidase (HRP)-conjugated anti-human IgG (Dianova, 709-035-149) and 1-step Ultra TMB or, in assays for concentration-dependent SARS-CoV RBD binding, 1-step Slow TMB (Thermo Fisher Scientific). The half-maximal effective concentrations (EC_{50}) were determined from non-linear regression models using GraphPad PRISM, version 9 (GraphPad). Selected purified mAbs were biotinylated and applied in ELISA-based epitope binning experiments as described.[1] Immobilized SARS-CoV or SARS-CoV-2 RBD-Fc were first incubated with non-biotinylated (competing) mAbs at 10 μg/ml for 15 min. After addition of one volume of biotinylated (detection) mAbs at 100 ng/ml, the

mixture was incubated for further 15 min. Binding of biotinylated mAbs was detected using HRP-conjugated streptavidin (Roche Diagnostics) and 1-step Ultra TMB.

Plaque reduction neutralization tests (PRNTs)

To quantitively evaluate the neutralizing activity of the mAbs, we performed plaque reduction neutralization tests (PRNT) as described before.[32] In brief, Vero E6 cells (ATCC) were seeded in 24-well plates at 1.6×10^5 cells/well and incubated overnight. The mAbs were diluted in 200 µl of OptiPro medium and mixed with 200 µL of OptiPro medium containing 100 PFU of the respective virus, either wildtype Munich isolate 984[32]) or VOC.[20,34] The mAb-virus mixture was gently vortexed, incubated at 37°C for one hour and then added to the Vero E6 cells for another hour at 37°C. The cell supernatants were then discarded, the cells washed once with PBS and supplemented with 1.2% Avicel solution in DMEM. After three days at 37°C, the supernatants were removed, the plates were fixed and inactivated using a 6% formaldehyde/PBS solution and stained with crystal violet. All dilutions were tested in duplicates. Non-linear regression models were determined for illustration using GraphPad PRISM, version 9 (GraphPad).

CHO cell line development

CHO DG44 cells (Invitrogen) derived from a GMP bank were cultured and transduced under serum-free conditions using lentivirus-derived vectors. After addition of lentiviral particles harboring expression constructs for hIgG1 mAbs, cells were incubated at 37°C and 5% CO_2 and maintained for 20 days on average. High producer clone pre-enrichment was performed using the MACSQuant Tyto® (Miltenyi Biotec), a sterile and closed system cell sorting platform. Briefly, a mAb-specific catch reagent was attached to the cell surface of all CHO cells. Secreted mAbs were specifically bound to the catch reagent on secreting cells and subsequently labeled with two mAb-specific secondary antibodies (Miltenyi Biotec), anti-hIgkappa conjugated to phycoerythrin (PE) as detection antibody and anti-hIgG1 conjugated to allophycocyanin (APC) for positive cell selection by MACSQuant Tyto. A two-fold limiting dilution with 0.5 cells per well was used for single cell cloning from enriched high producer cell pools to ensure monoclonality. Cells were cultured at 37°C, 5% CO_2, and 85% humidity for 14 to 20 days. Wells were analyzed regarding cell number, viability and expression level of the target mAb using IgG-ELISA Kit (Invitrogen) and Vi Cell XR cell counter (Beckmann Coulter). Selected clones were cryopreserved and tested accordingly to state of the art GMP guidelines.

mAb production and purification from CHO cells

Small scale production of human IgG1 mAbs were conducted in 1 liter batch cultures using 2 liter Erlenmeyer shake flasks. Isolated CHO DG44 producer clones were inoculated at a cell concentration of 2.5×10^5 cells/ml in ProCHO™ 5 protein-free medium (Lonza) and cultivated for 11 days in an orbital shaking incubator (Infors AG) at 95 rpm using a 50 mm diameter orbital at 37°C, 5% CO_2 and 85% humidity. Cell culture supernatant was collected and secreted mAbs were purified with HiTrap® MabSelect™ using an ÄKTA Purifier 10 System (both Cytiva). Briefly, the column was equilibrated with binding buffer, cell free supernatants were filtered (0.22 µm) and loaded onto the column (1–2 ml/minute). After washing with 10 CV of washing buffer, mAbs were eluted with 0.1 M citric acid, pH 3. Protein-containing fractions were pooled and rapidly neutralized to pH 7 using 1 M Tris/HCl, pH 8.0. Buffer was exchanged to PBS using PD-10 columns (Cytiva). Purified mAbs were analyzed by SDS-PAGE under reducing and non-reducing conditions stained with Coomassie Brilliant Blue, IEF, SEC, NanoDSF and intact mass determination.

Mass spectrometric analysis

Purified mAbs were incubated with PNGase F (Promega) to remove N-linked glycans and optionally also with DTT (12 mM for 15 min at 37°C) to separate heavy and light chains. Samples were separated using Agilent Zorbax Stable Bond SB300 C8 with a linear gradient of 0.1% formaldehyde, 80% n-propanol, 10% acetonitrile on an 1100 HPLC (Agilent) coupled with a Micro TOF Q-II mass spectrometer (Bruker Daltonics). Molecular weights were determined by charge deconvolution using the MaxEnt algorithm.

Surface plasmon resonance (SPR) measurements

The SPR measurements were performed on a Biacore T200 instrument at 25°C using a buffer containing 10 mM HEPES pH 7.4, 150 mM NaCl, 3 mM EDTA and 0.05% Tween 20. For RBD binding kinetic measurements, the SARS-CoV-2 S protein-RBD-mFc antigen (ACROBiosystems) was reversible immobilized on a C1 sensor chip via anti-mouse IgG capture surface. The tested mAbs were injected at different concentrations and the interaction analyzed as a multi-cycle-kinetic measurements in duplicates. The equilibrium

dissociation constant values (K_D) were determined using a monovalent analyte model. For ACE2 competition analysis a CAP sensor chip was coated with Biotin CAPture reagent before immobilization of biotinylated Avi-tagged ACE2 (ACROBiosystems). The interaction was analyzed after the addition of the His-tagged SARS-CoV-2 S protein-RBD antigen (ACROBiosystems) in the absence or presence of the tested mAbs at different concentrations. The mAb-concentration dependent ACE2-RBD response was analyzed with non-linear regression models using GraphPad PRISM, version 9 (GraphPad).

SARS-CoV-2 VOC solid phase binding assays

Binding of mAbs against RBDs of SARS-CoV-2 VOCs was assessed using a solid phase immunoassay (SeraSpot® Anti-SARS-CoV-2 IgG, Seramun Diagnostica GmbH) as described before.[20] Briefly, on the bottom of each well of 96 well plate, SARS-CoV-2 antigens (InVivo BioTech Services GmbH) and controls are printed in an array format. The RBD antigens (318–541) of the SARS-CoV-2 Spike protein were based on the wildtype sequence with added mutations as listed in parenthesis as indicated by the provider (https://www.invivo.de/sars-cov-2-antigens/): for RBD Alpha E484K (E484K, N501Y); for RBD Beta (K417N, E484K, N501Y); for VOC-Gamma (K417T, E484K, N501Y); and for VOC-Delta (L452R, T478K). Color intensity of immune complexes formed during the incubation at the site of each antigen spot was measured using a SpotSight® plate scanner with the color intensity correlating to the amount of bound antibodies.

Hamster model of a SARS-CoV-2 VOC infection

For the SARS-CoV-2 infection experiments, hamsters were randomly distributed into three groups. All animals were infected intranasally with 1×10^5 PFU of SARS-CoV-2, VOC Alpha (isolate BetaCoV/Germany/ChVir21652/2020, GISAID accession ID EPI_ISL_802995). The VOC Alpha virus integrity was verified via Next Generation Sequencing prior to animal experiments. A passage four stock was grown on Vero E6 cellsdiluted in minimal essential medium (MEM; PAN Biotech) to a final volume of 60 µl as previously described.[26] Animals of the first group (post-exposure) were given a single intraperitoneal (i.p.) injection of CV38-142 at a dose of 30 mg/kg 2 hours after viral infection. Animals of the second group (therapeutic) received the same mAb application 24 hours after infection. Animals of the third group (control) underwent the same procedure as post-exposure hamsters, but with difference of receiving a non-viral isotype-matched control mAb that is named a-KLH and that targets the metalloprotein Keyhole Limpet Hemocyanin (Miltenyi Biotec). Throughout the experiment, the body weights from all animals were recorded daily and their clinical status monitored twice daily. On 3, 5 and 7 dpi, three hamsters of each group were euthanized by exsanguination under general anesthesia after single 200 µl intramuscular injection containing 0.15 mg/kg medetomidine, 2 mg/kg midazolam and 2.5 mg/kg butorphanol.[42] Throat swabs and the right lung lobe were used for quantification of viral RNA and functional viral particles. The left lung lobes were carefully removed and immersed in fixative solution (4% formaldehyde, pH 7.0) for 48 hours before further processing for histopathological investigations.

Quantification of viral RNA and functional viral particles

From throat swabs and homogenates of 2.5 mg of lung tissue we extracted RNA using the innuPrep Virus DNA/RNA Kit (Analytik) following the manufacturer's instructions. For quantification of viral RNA a one-step RT qPCR reaction was conducted using the Luna Universal Probe One-Step RT-qPCR kit (New England Biolabs) and previously published TaqMan primers and probes (hamster RPL18 and SARS-CoV-2 E_Sarbeco).[35,43] To determine titers of functional viral particles, homogenates from 25 mg of lung tissue were serially titrated and added to Vero E6 cells in 12-well-plates. After 2.5 hours, cells were overlaid with MEM containing 1.5% carboxymethylcellulose sodium (Sigma Aldrich) for three days. Subsequently, the cells were washed with PBS, formalin-fixed, stained with crystal violet and plaques were quantified.

Histopathological examinations

Formalin-fixed lung tissues were embedded in paraffin and cut into 2 mm sections. Slides were dewaxed in xylene and rehydrated in decreasing ethanol concentrations, then stained with hematoxylin and eosin (HE). The stained slides were then scanned and microscopically (digital microscopy) evaluated by a board-certified veterinary pathologist who was blinded for group that the animal belonged to. The examination to assess the character and severity of pathologic lesions using lung-specific inflammation scoring parameters[44] was performed as previously described for SARS-CoV-2 infection in hamsters.[1,26] These parameters included the relative area and severity of interstitial pneumonia; the infiltration of immune cells subdivided in lymphocytes, macrophages, neutrophils and heterophils; and the extent of bronchial epithelial cell (BEC)

necrosis, BEC hyperplasia, bronchitis, bronchiolitis, hyaline membranes, alveolar epithelial cell (AEC) necrosis, AEC type II hyperplasia, alveolar edema, perivascular edema, perivascular lymphocytic cuffing (PLC), bronchus-associated lymphoid tissue (BALT), endothelialitis and alveolar hemorrhage (Table S2). Of those parameters three scores have been assessed as described previously[1,26]: (1) immune cell infiltration score that includes the infiltration of lymphocytes, macrophages and neutrophils and the extent of PLC; (2) lung inflammation score that includes the severity of interstitial pneumonia and the extent of BEC necrosis, of bronchitis and of AEC type II hyperplasia; and (3) the edema score that includes the extent of alveolar and perivascular edema.

Reactivity screening on murine tissues

8 to 12 weeks old C57BL/6J mice were sacrificed in isoflurane anesthesia to carefully prepare brain, lung, heart, liver, kidney and colon tissues, which were then immediately frozen in −50°C cold 2-methylbutane to cut 20 μm sections on a cryostat. Glass-mounted tissue slices were used for reactivity screening following established protocols.[1,31] In brief, unfixed tissues were rinsed with phosphate-buffered saline (PBS) then blocked with PBS containing 2% Bovine Serum Albumin (Roth) and 5% Normal Goat Serum (Abcam) for 1 hour at room temperature, before mAbs were added at 5 μg/ml and incubated at 4°C overnight. The slices were then washed three times with PBS, before a two hour incubation with a secondary goat anti-human IgG-Alexa Fluor 488 antibody (Dianova, 1:1000 in blocking solution). After another three PBS washing steps, the slices were mounted using DAPI-containing Fluoroshield (Abcam). Staining was examined under an inverted fluorescence microscope (Olympus CKX41, Leica DMI6000). As a control, we used the isotype-matched human mAb #011–138 which has been isolated from an autoimmune encephalitis patient[31] and which binds to human tissues.

Human membrane protein library screen

A commercial library-based Membrane Proteome Array (MPA) screening was conducted at Integral Molecular (Philadelphia, U.S.A.) to investigate for mAb binding to 6,000 distinct human membrane protein clones, each overexpressed in live cells from expression plasmids. Each clone was individually transfected in separate wells of a 384-well plate followed by 36 hours of incubation.[45] Cells expressing each individual MPA protein clone were arrayed in duplicate in a matrix format for high-throughput screening. Before screening on the MPA, the test concentration of CV38-142 for screening was determined on HEK-293T cells expressing positive (membrane-tethered Protein A and SARS-CoV-2 S1 RBD) and negative (mock vector-transfected) binding controls, followed by detection by flow cytometry using a fluorescently-labeled secondary antibody. The test concentration was chosen at 20 μg/ml with a background rate below 0.1% measured as average mean fluorescence intensity (MFI) in comparison to the vector control. CV38-142 was then added to the MPA at 20 μg/ml and binding across the protein library was measured on an Intellicyt iQue using a fluorescently labeled secondary antibody. Each array plate contains both positive (Fc-binding) and negative (empty vector) controls to ensure plate-by-plate reproducibility. CV38-142 interactions with any targets identified by MPA screening were confirmed in a second flow cytometry experiment using serial dilutions of the test ligand, and the target identity was re-verified by sequencing.

Human tissue cross-reactivity study

The human tissue crossreactivity study was performed in compliance with GLP requirements by a certified provider, TPL Path Labs GmbH (Freiburg, Germany). CV38-142 from CHO cell production and negative control antibody (#I5154, Sigma) were biotinylated using EZ-Link™ NHS-LC-LC Biotin (Pierce). Antibodies to be biotinylated were adjusted to 2.0–2.5 mg/ml in sodium bicarbonate buffer. The biotinylation reagent was prepared by dissolving Succinimidyl-6-(Biotinamido)-6-Hexanamid-Hexanoat in Dimethylsulfoxid (DMSO). Biotinylation reagent was mixed with the corresponding antibody in a molar ratio of 15:1, and the mixture was incubated for 1 hour at room temperature. Finally, the mixtures were purified to remove biotinylation reagent and stored in PBS buffer. Tissues from three different healthy donors were procured from two commercial vendors (Cureline and Tissue Solutions) and were stored at −80°C. Blood smears were prepared from TPL Path Labs GmbH and stored at room temperature in a dry environment. The tested tissues comprised adrenal gland, aorta (endothelium), blood cells smear, bone marrow, brain (cortex), brain (cerebellum), mammary gland, cervix, colon, duodenum, whole eye, anterior eye, posterior eye, heart (myocardium), ileum, jejunum, kidney (cortex), liver, lung, lymph node, central ovary, oviduct/fallopian tube, pancreas, parathyroid, parotid gland, peripheral nerve, pituitary gland, placenta, prostate, skin, spinal cord, spleen, stomach, striated skeletal muscle, testis, thymus, thyroid, tonsil, ureter, urinary bladder and uterus; complying with FDA and EMA requirements. For controls, HEK-293T cells either transfected

with SARS-CoV-2 S1 (positive control) or untransfected (negative control) were embedded in OCT medium (Roth). From blocks of human frozen tissues and control test systems serial sections were cut at 5 µm nominal thickness with a freezing microtome. The biotinylated antibodies were prepared to stocks of 0.5 µg/ml and 5 µg/ml in Ventana diluent (#760-108, Ventana) that were used for the entire study. Optimized immunohistochemical staining parameters were determined in a validation study and conducted on an automated Ventana Discovery Ultra platform. Sections were fixed with 1% PFA (Roth) in PBS for four minutes at room temperature, blocked 5% normal human serum (Invitrogen) for 32 minutes at room temperature and then stained with biontinylated CV38-142 or control antibodies for 1 hour at room temperature. Binding of antibodies was detected using a DAB Map detection system (#760-124, Ventana) before counterstaining with Hematoxylin II (#790-2208, Ventana) and Bluing reagent (#760-2037, Ventana). Positive and negative control stainings were performed in each immunostaining run to assure the quality and stability of the staining. Visualization of all stained sections was performed by light microscopy, using Zeiss Axioskop or A1 microscopes and evaluated for the distribution and intensity of staining by a certified pathologist. Images were cropped using ZEN2 software (Zeiss Microscopy) from digital whole section images acquired with an Axioscan Z1 slide scanner.

Characterization of RBD – mAb binding residues

The structural data was previously published of SARS-CoV-2 RBD in complex with CV38-142[19] (PDB: 7LM8) and Sotrovimab[17] (PDB: 7JX3), respectively. The epitope and paratope residues as defined by a buried surface area (BSA) greater than 0 $Å^2$, as well as their interactions as hydrogen bonds or salt bridges were identified using PDBePISA[29] (https://www.ebi.ac.uk/pdbe/prot_int/pistart.html).

RBD VOC ELISA

Binding of mAbs against RBDs of Omicron, wildtype, and wildtype with the N440K substitution was assessed by an ELISA. 96 well plates (Nunc Maxisorp, Roskilde, Denmark) were coated with 1 µg/mL anti-His (clone GG11-6F4.3.2, Miltenyi Biotec) and then blocked with PBS containing 1% BSA. SARS-CoV-2 Spike RBD of wildtype, VOC Omicron, and wildtype N440K (R319 to K537, ACROBiosystems), respectively, were added at 1 µg/mL for 1 hour at room temperature. CV38-142 was applied at 20 µg/mL to 1 ng/mL in duplicates and incubated for 1 hour at room temperature. Detection was performed by addition of anti-Fc-HRP (#A0170, Sigma) at 1:10,000 dilution and TMB (SERVA Electrophoresis). Non-linear regression models using GraphPad PRISM, version 9 (GraphPad) were applied to determine best fits and EC50 for binding.

QUANTIFICATION AND STATISTICAL ANALYSIS

Binding kinetics of mAbs to RBD were modeled from multi-cycle surface plasmon resonance measurements (Figures 2A–2C) using the Biacore T200 software, version 3.2. All statistical tests were performed using GraphPad PRISM, version 9 (GraphPad). For concentration-dependent mAb binding using ELISA (Figures 5A and S1A) and for concentration-dependent neutralization of plaque formation from authentic SARS-CoV-2 isolates (Figures 2F–2H, 5B, 5C, S1C, and S2A–S2C) and for concentration-dependent ACE2-competition assay using SPR (Figure 2D) non-linear regression models were determined. For bodyweight changes from hamster experiments (Figure 3B), a D'Agostino-Pearson normality test revealed normal distribution. Thus, statistical significance of bodyweight changes from hamster experiments was tested using a mixed-effects model (two-way ANOVA) with posthoc Dunnett's multiple comparisons test in comparison to control group. Statistical details can be found in the figure legends.